

NUCLEAR ENHANCED MHD MEGAWATT SPACE TRANSPORT

By

ARLO JEFFREY SWALLOW

A THESIS PRESENTED TO THE GRADUATE SCHOOL  
OF THE UNIVERSITY OF FLORIDA IN PARTIAL FULFILLMENT  
OF THE REQUIREMENTS FOR THE DEGREE OF  
MASTER OF SCIENCE

UNIVERSITY OF FLORIDA

2009

© 2007 Arlo Jeffrey Swallow

To my mother and father

## ACKNOWLEDGMENTS

I would like to acknowledge Dr. Anghaie for providing much needed help and guidance throughout the better part of my work on this project and whose positive attitude always helped lessen any stresses I had. I would also like to thank Dr. Dugan and Dr. Tulenko who were both willing to serve as members of my thesis committee on short notice.

## TABLE OF CONTENTS

	<u>page</u>
ACKNOWLEDGMENTS.....	4
LIST OF TABLES.....	8
LIST OF FIGURES .....	9
ABSTRACT .....	11
 CHAPTER	
1 INTRODUCTION.....	13
Space Transport Vehicle.....	13
Spacecraft Power and Mass.....	14
Solar Power .....	14
Nuclear Power.....	14
Electric Power Conversion .....	14
Turbogenerators .....	14
Magnetohydrodynamic Generators .....	15
Power density and temperature problem .....	15
Nuclear enhanced ionization .....	16
System Description .....	16
Rubidium Closed Cycle.....	16
Closed Cycle Description.....	17
Additional Spacecraft Components .....	17
Focus and Objectives .....	17
2 MHD GENERATOR.....	20
MHD Generator Description .....	20
MHD Modeling .....	20
Rubidium Thermal Properties.....	23
Rubidium Saturation Curve.....	24
MHD Power Density.....	24
Magnetic Field .....	25
Velocity .....	25
Electric Conductivity.....	26
Thermal ionization .....	27
Nuclear enhanced ionization of rubidium.....	28
Rubidium activation and decay .....	29
MHD Generator Mass.....	29

3	SQUARE LATTICE HONEY COMB REACTOR.....	33
	Reactor Description.....	33
	Core Description .....	33
	Reflector and Control Drums .....	33
	Neutronic Modeling .....	34
	Material Cross Sections.....	35
	K-code .....	36
	Mesh Tallies.....	36
	True Fluxes and Power.....	36
	Burnup .....	37
	Thermal Hydraulic Analysis.....	38
	Two Phase Flow Effects.....	39
	Liquid Phase Temperature and Pressure Modeling.....	40
	Two Phase Temperature and Pressure Modeling .....	41
	Vapor Phase Temperature and Pressure.....	42
	Heat Transfer Coefficients .....	43
	Critical Heat Flux .....	43
	Fuel Temperature.....	44
	Reactor Mass Estimate.....	45
4	OTHER SPACECRAFT COMPONENTS .....	49
	Nozzle and Diffuser .....	49
	Thermal Hydraulic Modeling.....	49
	Mass Estimate .....	49
	Condensing Radiator.....	50
	Thermal Hydraulic Modeling.....	50
	Mass Estimate .....	51
	Pump .....	51
	Thermohydraulic Modeling .....	51
	Mass Estimate .....	51
	Power Management and Distribution System .....	52
	Radiation Shield .....	52
	Radiation Damage Limits.....	52
	Shadow Shield .....	53
	Neutron shielding .....	53
	Gamma shielding.....	53
	Shield Modeling and Mass Estimate .....	54
	Supporting Structure .....	54
	Propellant and Orbital Mechanics Model .....	54
5	RESULTS AND FINAL SPACECRAFT DESIGN .....	58
	MHD Power.....	58
	Effect of Core Exit Temperature .....	58
	Effect of Core Exit Pressure.....	58

Effect of Mass Flow Rate.....	59
Flow Area Design Change .....	59
Core Thermal Hydraulic Results.....	60
Excessive Fuel Temperature .....	60
Heat Transfer Design Change .....	61
Reactor Neutronic Results .....	62
Fuel Loading and Criticality .....	63
Flux Profiles .....	63
Linear Heat Generation Rate.....	64
Burnup .....	64
Shadow Shield .....	65
Closed Cycle Thermal Hydraulic Results.....	65
Spacecraft Mass and Specific Power .....	67
 6: CONCLUSION .....	 77
Thermal Hydraulics.....	77
Fuel Effects.....	78
Mass and Power. ....	78
Future Work.....	78
 APPENDIX: MATERIAL ISOTOPE CONCENTRATIONS .....	 80
 LIST OF REFERENCES .....	 83
 BIOGRAPHICAL SKETCH .....	 85

## LIST OF TABLES

<u>Table</u>		<u>page</u>
5-1	k effective both with and without control for different fuel loadings.....	75
5-2	Cycle parameters for various fuel loadings .....	75
5-3	Cycle component temperature, pressure and associated power .....	75
5-4	Mass and specific mass for each system component .....	76

## LIST OF FIGURES

<u>Figure</u>	<u>page</u>
1-1 Diagram of rubidium closed loop MHD cycle .....	19
2-1 Diagram of vector components within an MHD Generator. ....	31
2-2 Rubidium Liquid-Vapor Saturation Curve .....	31
2-3 Amount of Rb-88 and Activity of Rb-88 per gram of Rubidium-87 vs. time within a closed cycle loop. ....	32
3-1 Arrangement of tri-carbide fuel to form a fuel sub assembly in the SLHC reactor.....	46
3-2 Cross-sectional view of original SLHC reactor .....	46
3-3 1/Sixth MCNP model of SLHC reactor .....	47
3-4 Axial view of SLHC reactor depicting fuel regions based on changes in rubidium density .....	47
3-5 Visual depiction of the fuel heat transfer models.....	48
4-1 High temperature low mass radiating condenser design .....	56
4-2 Angular protection provided by a shadow shield.....	57
5-1 Core exit Mach number and MHD for original SLHC design for various core exit temperatures.....	68
5-2 Effect of core exit pressure on core Mach number and MHD power both with and without expansion for the original SLHC.....	68
5-3 Core exit Mach number and MHD power for original SLHC design for various mass flow rates.....	69
5-4 Effect of mass flow rate on core exit Mach number and MHD power for the radially-increased SLHC and with 50% cross-sectional flow area within the fuel.....	69
5-5 Core temperature profiles for radially-increased SLHC with 2 mm fuel wafer thickness for constant LHGR. ....	70
5-6 Axial core temperatures for radially-increased SLHC with 1 mm thick fuel wafers .....	70
5-7 Radially-increased SLHC MCNP model.....	71
5-8 Thermal (0 to 1.86 eV) neutron flux for each fuel type at 6 MW .....	71

5-9	Total flux at 6 MW for each fuel type .....	72
5-10	LHGR for sub fuel assembly .....	72
5-11	$k_{\text{eff}}$ with fuel depletion for the three different uranium concentrations. ....	73
5-12	LiH shadow shield at the end of the reactor. ....	73
5-13	LEO to GEO round trip duration and liquid hydrogen consumption vs. starting propellant amount.....	74

Abstract of Thesis Presented to the Graduate School  
of the University of Florida in Partial Fulfillment of the  
Requirements for the Degree of Master of Science

NUCLEAR ENHANCED MHD MEGAWATT  
SPACE TRANSPORT

By

Arlo Jeffrey Swallow

May 2009

Chair: Edward Dugan  
Major: Nuclear Engineering

A system analysis of the Square Lattice Honey Comb (SLHC) reactor with a magnetohydrodynamic (MHD) generator using liquid/gaseous rubidium in a direct closed Rankine cycle was conducted to assess the design feasibility in a satellite transport. Radiation induced ionization enhances electric conductivity of the working fluid in MHD generators and increases the electron temperature in the Magnetoplasmadynamic (MPD) thruster. The enhancement of the partially ionized plasma properties is well above what is obtained under equilibrium condition, which is dictated by pressure and temperature of the gas. The nonequilibrium enhancement of the conductivity is the key factor in achieving performance characteristics that are well above the state-of-the-art MHD generators or MPD thrusters.

The square lattice honey comb reactor is a very compact reactor originally developed for nuclear thermal propulsion and uses highly enriched tri-carbide fuel (U,Zr,Nb)C and a zirconium hydride moderator. Rubidium is used as a coolant due to its activation and decay properties that enhance the electric conductivity of the rubidium vapor within the MHD generator. The exit flow conditions of the rubidium coolant are determined based off the performance requirements of the MHD generator and necessitates enlarging the core radially by a factor of 1.5 from the original design. MCNP-X is used to model the reactor and ascertain  $k_{\text{eff}}$  (both with and without

control drums), the axial flux profile, and burnup. Rubidium properties throughout the system are determined and the homogenous two phase flow model is used in the reactor.

Results indicate a spacecraft design with nearly 1 MW of electric power which could produce that power at 7.0 kg/kWe. Based on the reactor burnup, the satellite transport could operate at full power for nearly 5.5 years and result in a usage spacecraft lifetime of 7 years or more.

## CHAPTER 1 INTRODUCTION

### **Space Transport Vehicle**

A space transport vehicle is an autonomous spacecraft capable of performing a variety of functions. One of the biggest functions space transports could provide is a means to manage the Earth's rapidly growing artificial satellite network. As of 2008, there were approximately 800 active satellites in Earth orbit with over 50% belonging to the United States. According to Galabovat et. al (2003), space transports could perform a variety of missions including rescuing satellites falling out of optimal orbits, assembling large scale space systems such as space stations, on demand military satellite repositioning, removing retired geostationary satellites from their valuable orbit space and much more.

One very important mission, on which part of this study is based, is the transport of satellites destined for geosynchronous orbit (GSO) from a low earth orbit (LEO). Investigation done by Futron Corporation to evaluate the average cost to launch payloads to various orbits found (as of the year 2000) it cost nearly \$27,000/kg to launch satellites to GSO orbits, whereas it only cost about \$11,000/kg to launch satellites to LEO (Futron Corporation, 2002). With an average GSO satellite mass of 4500 kg and nearly 200 commercial GSO satellites launched in a ten year period, the extra cost in launching those satellites directly to GSO is approximately \$13.9 billion. Therefore, even if a space transport cost as much as \$1 billion dollars to build and put up into space, the savings to the GSO satellite community would amount to over a \$ 1 billion per year of operation.

## **Spacecraft Power and Mass**

### **Solar Power**

Spacecraft power and mass are two of the most important factors in a spacecraft design. A transport capable of ferrying a satellite to GSO and returning back to LEO in a reasonable amount of time (less than a month) requires an electric power of a megawatt or more. The most common power source used today in an around earth orbit is solar cells. Solar cells used in space can achieve 30-40% efficiencies; however, they are limited by the amount of energy arriving from the sun per unit area. The average solar energy flux near the earth is  $1360 \text{ W/m}^2$  which means a solar powered 1 megawatt spacecraft would need over  $1800 \text{ m}^2$  of solar cells. The current specific mass for solar cell technology is approximately  $30 \text{ kg/kWe}$  (Litchford, 2001). Solar power designs call for very large and massive transports not just because of the size of the solar array, but also for the batteries which are needed when the spacecraft is in the Earth's shadow.

### **Nuclear Power**

Nuclear powered spacecraft have the capability of producing large amounts of power for relatively little mass and can operate at full power independent of the sun. Additionally, the power of a nuclear reactor is limited only by the ability to adequately remove heat from the core in order to prevent melting or other material failure. Therefore, very large power densities are feasible with nuclear reactors.

## **Electric Power Conversion**

### **Turbogenerators**

Unlike solar power where the energy of the sun is converted relatively directly into electrical power, nuclear power requires a much more complex system to convert the thermal power of the reactor into electrical power. Almost all terrestrial nuclear power uses a form of the

steam cycle and steam generators to convert the thermal power of the reactor into electrical power. However, turbogenerators operate most effectively at low temperatures. High temperatures in a turbogenerator cycle are difficult if not impossible because of the material limitations of the turbine blades when exposed to heat and rotational forces.

Radiators, which offer the only means to remove heat from a spacecraft, remove heat proportional to  $T^4$ . Low heat rejection temperatures require significantly larger radiator surface areas and in turn masses to remove the same amount of heat as high heat rejection temperatures. For systems that create several megawatts of thermal power that must be radiated away, the radiator can easily become the most massive component of the spacecraft. According to Litchford (2001), due to the low temperatures of turbogenerator cycles, spacecraft employing these systems are unlikely to achieve specific mass much below 10 kg/kWe. Therefore, a high temperature cycle rejecting heat at high temperatures is desired to reduce spacecraft specific mass.

### **Magnetohydrodynamic Generators**

Magnetohydrodynamic (MHD) generators appear to offer the best solution for space based electrical power conversion. They create electrical energy by passing an electrically conductive fluid through a magnetic field. The magnetic field creates a force on the free electrons within the fluid and a flow of electrons or current is created. With no moving parts, MHD generators can be designed to withstand much higher temperatures than turbogenerators. Additionally, MHD generators are capable of achieving very large power densities which enable designs that are relatively small in size and mass.

### **Power density and temperature problem**

However, the power density of an MHD generator is a function of the working fluid's electric conductivity. A principal challenge to overcome with MHD generators is that they

require an ionized gas with sufficient electric conductivity (10 mho/m or greater). Thermally excited plasmas require temperatures of 3000 K or greater to achieve this degree of electric conductivity (Rosa, 1968). Although a high temperature heat rejection cycle is sought, the maximum temperature of the cycle is limited by the material properties of the reactor which heats the gas. With this upper limit on temperature, the thermally induced electric conductivities remain low and compact MHD generators cannot be built to meet the needs of spacecraft.

### **Nuclear enhanced ionization**

There are, however, methods to increase the electric conductivity of gases beyond what can be achieved through thermal ionization. One very promising method for a nuclear powered spacecraft is using radiation enhanced ionization. When a neutron is captured by an atom it becomes a more massive isotope of that same element. Many isotopes are unstable and will decay—transforming into a different element and releasing radiation in the process. In the case of a beta decay, where the released radiation is in the form of an electron, the electric conductivity of the gas is increased. Additionally, if the electron is released with sufficient energy it can proceed to strip electrons off other atoms in the fluid and increase the electric conductivity further. Therefore, ionizing a gas to produce sufficient electric conductivity can be done without extreme temperatures.

## **System Description**

### **Rubidium Closed Cycle**

The purpose of this study was to assess the feasibility of using rubidium in the square lattice honey comb reactor with an MHD and the characteristics of a space transport based on that system. Neutronic and thermal properties suggest rubidium-87 is the best alkali metal to serve as a working fluid of a reactor utilizing nuclear enhanced ionization for an MHD generator with expected electric conductivities around 100 mho/m. The square lattice honey comb (SLHC)

reactor was originally designed at INSPI for nuclear thermal propulsion which requires no electrical conversion method. Therefore, much of the work done is ascertaining how the reactor works in a closed loop system.

### **Closed Cycle Description**

A schematic diagram of SLHC/MHD direct Rankine cycle power plant is provided in Figure 1-1. Liquid rubidium near liquid saturation will be pumped into the reactor. As the rubidium coolant traverses the core, heat is removed from the core and in turn the liquid rubidium becomes superheated rubidium vapor. The flow is then expanded through a nozzle/MHD generator to achieve maximum generator performance with respect to both efficiency and power-to-mass ratio. After passing through the MHD generator, the exhaust will be diffused to low speeds and enter a condensing radiator. In the radiator, the rubidium vapor will be condensed back to a liquid and then pumped back into the core to close the cycle.

### **Additional Spacecraft Components**

In addition to the components described in the rubidium loop there are four other system components that will be considered for the spacecraft mass estimate: the power management and distribution system (PMAD), propellant, shadow shield, and supporting structure. Although a small fraction of the power generated in the MHD generator supplies the power for the spacecraft bus as well as the power for the pump, the vast majority of the power will operate the PMAD with a magnetoplasmadynamic thruster. The shadow shield serves to protect the spacecraft and any payload from radiation escaping the reactor.

### **Focus and Objectives**

The focus of this spacecraft system design centers around four principal and interdependent features of the system: the MHD generator, steady state neutronic analysis of the

SLHC reactor, thermal hydraulic analysis of the entire system, and spacecraft component mass estimates.

Optimal operating conditions of the SLHC/MHD closed cycle system were investigated to achieve approximately 1 megawatt of electric power. Limitations on MHD generator performances were also discovered. This study investigated what design changes to the square lattice honey comb reactor were needed to achieve optimal system performance. Factors influencing reactor design included meeting optimal flow characteristics for the MHD generator, not exceeding reactor temperature limits, and maximizing burnup while still maintaining adequate control at beginning of life. Additionally, two phase thermal hydraulic analysis was performed within the reactor and radiating condenser. Ultimately the system's electric power, efficiency and total mass are sought to evaluate the effectiveness of the spacecraft as a space transport vehicle.

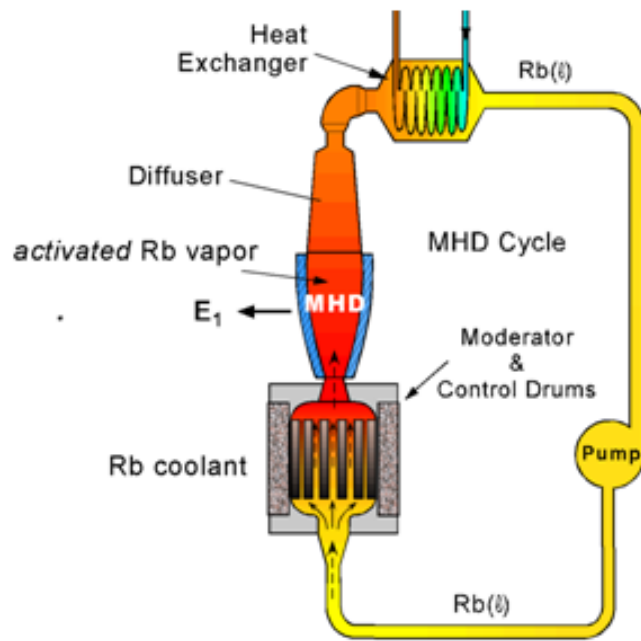


Figure 1-1. Diagram of rubidium closed loop MHD cycle

## CHAPTER 2 MHD GENERATOR

### **MHD Generator Description**

The MHD generator is the component of the spacecraft that converts the thermal power of the reactor into electrical power. Like all mechanical-to-electrical energy conversion methods, a magnetohydrodynamic generator operates by moving an electric conductor through a magnetic field. This creates a force on charged particles perpendicular to both the velocity of the conductor and the magnetic field and ultimately leads to the flow of electric current. However, unlike traditional generators which use a solid conductor rotating between the poles of a magnet, MHD generators employ an electric conducting fluid moving through a magnetic field.

For space applications MHD generators have several appealing features. According to Mitchner (1973), MHD generators can operate with extreme power densities of about 10 MW per cubic meter as long as the electric conductivity is 10 mhos per meter or greater . This in turn allows MHD generators to be built at sizes and masses well suited for spacecraft where volume and mass must be limited. Another advantage is that MHD generators require no moving mechanical parts allowing for higher temperatures within the MHD generator. Moving mechanical parts also have tendencies to fail over long operational periods. Repairing spacecraft, if possible, is very expensive and therefore, an MHD generator with no mechanical moving parts has fewer modes of failure. Additionally, reciprocating Machinery, which is not present in MHD generators, can have significant negative effects on spacecraft stability.

### **MHD Modeling**

The MHD generator in this system was modeled as a segmented Faraday generator. Faraday generators are the most limited in terms of electric efficiency. Currently the MHD generator that offers the best potential for use for a nuclear powered space system is the disk

MHD generator. Disk MHD generators can obtain the highest efficiencies as well as the lowest masses among all other MHD generator types. However, the decision to model the MHD generator in this system as a segmented Faraday generator was because this is a preliminary system design and the segmented Faraday generator is simpler to model. Additionally, many of the assumptions that follow serve to increase efficiency making the system performance more like that of a system using a disk MHD generator.

A schematic drawing of the vector components within a segmented Faraday generator is provided in Figure 2-1. A magnetic field perpendicular to the flow of the electrically conductive rubidium vapor generates a current which is perpendicular to both the flow velocity and the magnetic field. Neglecting the Hall effect, the current density is given by the generalized Ohm's Law as

$$\bar{J} = \sigma(\bar{E} + \bar{u} \times \bar{B}) \quad (2-1)$$

Hall effect is the result of current flowing in the y direction through the magnetic field generating a current flowing in the x-direction. In a single circuit Faraday generator there is a closed-circuit path for the Hall current to flow in the axial direction. The Hall effect ultimately reduces the current in the y direction and in turn the power density of the MHD generator. If the Faraday generator is infinitely segmented with many electrode pairs with separate loads, there remains no axial closed-circuit path for the Hall current and therefore, the Hall effect is eliminated. In practical applications finite segmentation of electrodes can sufficiently lower the Hall effect as long as the Hall parameter is kept below 2 (Rosa, 1968). This analysis idealizes segmentation and neglects the Hall effect and therefore the current density can be written as

$$J_y = \sigma(E_y - uB) \quad (2-2)$$

The electric power delivered to the load per unit volume of the generator is

$$P = -\bar{J} \cdot \bar{E} = |JE| \quad (2-3)$$

The force per unit volume that impedes the motion of the gas in the generator is given by

$$F = \bar{J} \times \bar{B} = -JB \quad (2-4)$$

A non-dimensional parameter called the loading parameter,  $K$ , defined as the ratio of the load resistance to the sum of the load resistance and the internal resistance is defined as.

$$K = \frac{E_y}{uB} \quad (2-5)$$

where  $0 \leq K \leq 1$ . This allows the power density and the force per unit volume to be written respectively as

$$P = K(1 - K)\sigma u^2 B^2 \quad (2-6)$$

$$F = (1 - K)\sigma u B^2 \quad (2-7)$$

where  $\sigma$  is the electric conductivity of the gas,  $u$  is the velocity of the gas, and  $B$  is the magnetic field strength. It can be shown from Equation 2-6 that the maximum power density for an ideal Faraday MHD system occurs when  $K=1/2$ . Therefore, a loading parameter of 0.5 was used in the MHD generator model.

The fluid equations for one-dimensional, steady state, inviscid, compressible flow without heat transfer within a Faraday generator can be written as

$$\rho u \frac{du}{dx} + \frac{dp}{dx} = \bar{J} \times \bar{B} = F \quad (2-8)$$

$$\rho u \frac{d}{dx} \left( \frac{u^2}{2} + h \right) = \bar{J} \cdot \bar{E} = -P \quad (2-9)$$

$$\rho u A = \text{constant} \quad (2-10)$$

According to Rosa (1968), assuming constant velocity in an MHD generator is often a good approximation. This assumption results in the fluid equations simplifying further as follows.

$$\frac{dp}{dx} = F \quad (2-11)$$

$$\rho u \frac{dh}{dx} = -P \quad (2-12)$$

$$\rho A = \text{constant} \quad (2-13)$$

The constant velocity assumption also results in the power density and force density becoming constants throughout the entire volume of the MHD generator when the electric conductivity and magnetic field strength are assumed constant as well. With the assumption of constant scalar electric conductivity and some manipulation, pressure and temperature between two points in the MHD can be related through

$$\frac{p_1}{p_2} = \frac{T_1^{\frac{\gamma}{\gamma-1}}}{T_2^{\frac{\gamma}{\gamma-1}}} K \quad (2-14)$$

where  $\gamma$  is the adiabatic exponent. The incremental length between the two points is given as

$$dx = \frac{p_1}{F} \left( 1 - \frac{p_2}{p_1} \right) \quad (2-15)$$

The constant velocity MHD generator equations are used to calculate the incremental generator length and pressure drop given a set temperature drop. The geometry of the MHD generator is that of a cylindrical duct. The radius at each segment is updated to satisfy continuity in Equation 2-13. Power per segment was calculated based on segment volume and power density. After each incremental calculation the thermal properties were updated and the next incremental calculation was conducted. The MHD calculations were terminated when the gas was expanded to the point of becoming a saturated vapor.

### **Rubidium Thermal Properties**

In order to perform thermal hydraulic analysis in all system components including the MHD generator, properties of rubidium were needed. Rubidium, like all other alkali metals, exists as a solid at room temperature and standard pressure. Although some alkali metals have been studied extensively at high temperature and pressure, especially sodium, relatively little

work has been done on collecting thermodynamic properties of both liquid and gaseous rubidium under these conditions. Ultimately, all property data were taken from the book compiled by Vargaftik (1975), which provided some thermodynamic data for rubidium at pressures up to 1 MPa and temperatures up to 3000 K. However, many properties such as viscosity and thermal conductivity were only available at lower temperatures and pressures and had to be estimated for temperatures above 1500 K based on linear relationships with temperature.

### **Rubidium Saturation Curve**

A saturation line was also developed to mark the transition between the liquid and gaseous phases of rubidium. Figure 2-2 shows this saturation curve. This curve determines the operating regimes for the pump, MHD generator, and diffuser as well as phase changes within the reactor and condenser.

### **MHD Power Density**

The relationships in Equations 2-14 and 2-15 indicate that the maximum amount of electrical energy that can be created is dictated by properties of the gas entering the MHD generator and not the properties of the MHD generator itself. This assumes that there exists some fluid velocity, a normal magnetic field, and electric conductivity, however small. In a simple sense this can be understood by the fact that energy is put into the gas through the thermal power of the reactor and any electrical energy created in the MHD generator must be extracted from the gas. However, the properties of the MHD generator do play a very large role in determining the MHD generator size and mass to extract that energy.

Achieving a very large power density is essential for a spacecraft system. The electric power density for an ideal MHD generator is proportional to  $\sigma u^2 B^2$ . Therefore, maximizing power density is accomplished by increasing the gas's electric conductivity, velocity, and the magnetic field strength within the generator.

## **Magnetic Field**

Since the magnetic field strength is squared in both the power density and force density equations, increasing the magnetic field can have a substantial impact on the generator size with virtually no change in the total amount of electrical energy extracted. The magnetic field in the MHD generator is a function of magnet size as well as generator size. The magnetic field is typically generated by coil windings and the magnetic flux density falls off with distance from the coils as  $1/r^2$ . For small MHD generators applicable for this system design, the radial distance is small enough to assume the magnetic field is constant within the working portion of the MHD generator. In larger power systems, design would either necessitate dealing with a magnetic field that varies or separating the flow into several smaller streams each with a smaller MHD generator.

Copper windings due to their limited current density of  $10^6$  A/m<sup>2</sup> can only create a magnetic field strength of about 1 Tesla before creating an extremely massive MHD generator. Near term magnets created from super conducting materials are expected to achieve magnetic fields around 8 Tesla according to Litchford (2001) without excessive weight. Magnetic fields of significantly greater strength in an MHD generator will be difficult to achieve anytime soon due to limits on current density within the superconducting windings. For this study, a magnetic field strength of 4 Tesla was used for the entire volume of the MHD generator.

## **Velocity**

The velocity of the fluid within the MHD generator has a dramatic influence since it is squared in the power density equation. However, the velocity of the gas is also a function of how much energy is in the gas, and therefore, increasing the velocity (assuming pressure and temperature are not affected) not only increases power density, but total power as well.

The velocity of the gas can be increased in two ways. One is by the amount of heating and/or increasing mass flow rate through the reactor which has a fixed cross sectional flow area. Ultimately, this process is limited by choked flow conditions and therefore, flow speeds exiting the reactor greater than  $M=0.7$  are not considered.

The velocity of the conductive gas can also be increased by expanding the flow through a nozzle. This process transforms stored energy in the form of pressure and temperature into kinetic energy. Maximum velocity limits are typically on the order of a few Mach due to limits on the back pressure of the nozzle as well as nozzle size. However, when a flow is expanded the pressure and temperature decrease. Therefore, depending on the gas properties, a gas can start to condense after sufficient levels of expansion and limit the maximum velocity. Additionally, when the flow condenses electrical power can essentially no longer be generated, and this decreases generator efficiency.

### **Electric Conductivity**

Maximizing electric conductivity is the final and most difficult parameter to achieve high power densities. Electric conductivity is the ability of the material to conduct electric current and has inverse units of resistivity. The flow of current requires free ions or electrons to carry the current. Good conductors such as solid copper have electric conductivities on the order of  $10^6$  mho/m. This is because atoms in solid metals exist relatively close together in a lattice and because of the low ionization energy of metals the electrons are relatively free to flow through the lattice. Electric conductivities in gases are generally lower by many orders of magnitude. This is due partly to the low density of gases where there are fewer ions per unit volume for the current to flow through.

In order to generate free electrons in a gas for current to flow through, atoms in the gas must be ionized. Ionization is the process of stripping an electron from an atom so that a free

electron and positive ion are created. Different elements have different minimum energies to remove an electron called ionization energies. Virtually all elements that exist as gasses under standard conditions like oxygen, nitrogen, and the noble gases have ionization energies between 12 to 20 eV/atom.

### **Thermal ionization**

Thermal ionization is the process of ionizing a gas by adding energy to the atoms by increasing the gas's temperature. Thermal ionization is described by Saha's equation which determines the populations of electrons and ions based on the gas temperature and ionization energy of the species in the gas (Mitchner, 1973). Thermal ionization is a process where the electrons, ions, and neutral particles of the gas are in thermal equilibrium at the gas temperature. Therefore, the rate of an electron re-binding with an atom is equal to the rate of ionization. Additionally, thermal ionization increases as does electric conductivity as the gas temperature is increased.

Achieving high electric conductivities through thermal ionization requires very high temperatures. Argon, for example, has an ionization potential of 15.7 eV and requires a temperature in excess of 6000 K to achieve an electric conductivity of 1 mho/m. Due to these very high temperatures, numerous studies have investigated seeding the gas with a small percent of a low ionization potential species such as an alkali metal. Alkali metals typically have ionization energies between 4 to 6 eV. In the case of 0.55 percent cesium added to argon, the temperature required to achieve an electric conductivity of 1 mho/m drops to 1500 K (Rosa, 1968). However, to achieve the power density necessary for a space system, the electric conductivity must be anywhere from 10 to 100 times greater and would require the seeded gas to remain at 2000 K or higher throughout the entire length of the MHD generator. This results in

very little power extraction since the gas can't be expanded to drop below 2000 K or requires the entrance temperature be a great deal higher which would exceed material limitations.

### **Nuclear enhanced ionization of rubidium**

Electric conductivity is proportional to the temperature of the electrons in the gas. In thermal ionization the temperature of the electrons is the temperature of the gas. However, in non-equilibrium ionization, the electrons can have a different temperature than that of the heavy particles making up the gas. Non-equilibrium ionization describes all processes where the energy of the electrons within the gas is not equivalent to the energy of the gas. That is to say the temperature of the electrons is not in equilibrium with the gas temperature (Rosa, 1968).

Ionizing radiation is by definition high energy particles or rays that ionize atoms. This allows for generation of free electrons independent of gas temperature. However, because the electrons are not in thermal equilibrium if the gas is no longer exposed to the ionizing radiation, the rate of recombination will exceed the rate of ionization and the gas will become less ionized. In the case where neutrons from the reactor are directly ionizing the gas, once the gas passes through the reactor it will begin to become less ionized and lose its electric conductivity.

There is another method of using nuclear radiation to create an ionized gas with an electric conductivity that remains relatively constant through the loop. This involves gas particles capturing neutrons from the reactor and transmuting into beta emitters. Beta emitters are unstable isotopes that will eventually decay and release a high energy electron known as a beta particle. These high energy beta particles not only increase the electric conductivity of the gas because they are free electrons, but also because they have high energy, they ionize other atoms in the gas increasing the electric conductivity further. Additionally, since the decay of an unstable isotope occurs at a random but probable time after becoming unstable, the gas can be exposed to a relatively constant amount of ionizing radiation as it passes through the entire

system loop. This allows for an equilibrium condition to exist after the coolant has been running through the loop for some set period of time.

### **Rubidium activation and decay**

Rubidium-87 was chosen to be the working fluid of this nuclear enhanced system because the average energy of the beta particle (2.07 MeV) emitted from the activated rubidium - 88 atom is at least four times larger than the average beta emission energy of any other activated liquid metal. Additionally, rubidium has a low ionization energy of 4.18 eV/atom and with a reasonable cross section of 0.12 b at thermal energies and a resonance integral of 1.9 b. Previous studies done by Anghaie (2007) modeling rubidium exposed to a neutron flux of  $10^{14}$  n/(cm<sup>2</sup>-s) found that the ratio of activated rubidium to non-activated rubidium was well above  $10^{-7}$  in less than 18 minutes. This was based on the assumption that rubidium would be exposed to the flux for 5 seconds in the core and would have a total cycle time of 60 seconds before it would reenter the reactor. Equilibrium levels of activated rubidium to unactivated rubidium versus time can be seen in Figure 2-3. The corresponding electron temperature from all these 2.07 MeV beta decays was estimated to be  $2.30 \times 10^{10}$  K. Therefore, non-equilibrium electric conductivity of the rubidium vapor was estimated to exceed 10 mho/m at a gas temperature of 800 K and to exceed 100 mho/m at 1500 K (Anghaie, 2007). These temperatures are easily manageable and electric conductivities of this level allow for design of an MHD generator compact enough to meet weight requirements for a spacecraft. For this study, a scalar conductivity of 100 mho/m was used within the working volume of the MHD generator.

### **MHD Generator Mass**

The mass of the MHD generator is almost entirely based on the magnet generating the magnetic field. The magnet is the sum of the coils and the supporting structure that must be

strong enough not to collapse under the very large magnetic field. The mass of the supporting structure is given by

$$m_{st} \geq \frac{\rho B^2 V}{S_t 2\mu_0} \quad (2-17)$$

where  $\rho$  is the density of the supporting material,  $S_t$  is the accepted strain,  $V$  is the volume of the MHD generator, and  $\mu_0$  is the permeability of free space (Litchford, 2001). Fiber reinforced composites have  $S_t/\rho$  values between 10 and 50 kJ/kg. Titanium has a ratio of 309 kJ/kg. For this study a very conservative  $S_t/\rho$  ratio of 10 was used, and therefore, the use of materials like titanium would result in supporting structures that would be more than 10 times less massive (Litchford, 2001).

The mass of the coil, which in many cases dominates the mass of the system, can be expressed by

$$m_c = \frac{\sqrt{2}\pi\rho_c B D^2}{\mu_0 j_c} \quad (2-18)$$

where  $D$  is the average diameter of the MHD generator and  $j_c$  is the accepted maximum current density of the coil material. Using coil materials, such as copper, that have current densities of the order  $10^6$  A/m<sup>2</sup> makes the mass of the coils extremely large. However, according to Litchford (2001), near term superconductors can sustain current densities as high as  $10^9$  A/m<sup>2</sup>. A conservative current density of  $10^7$  A/m<sup>2</sup> was assumed for the mass calculation of this study.

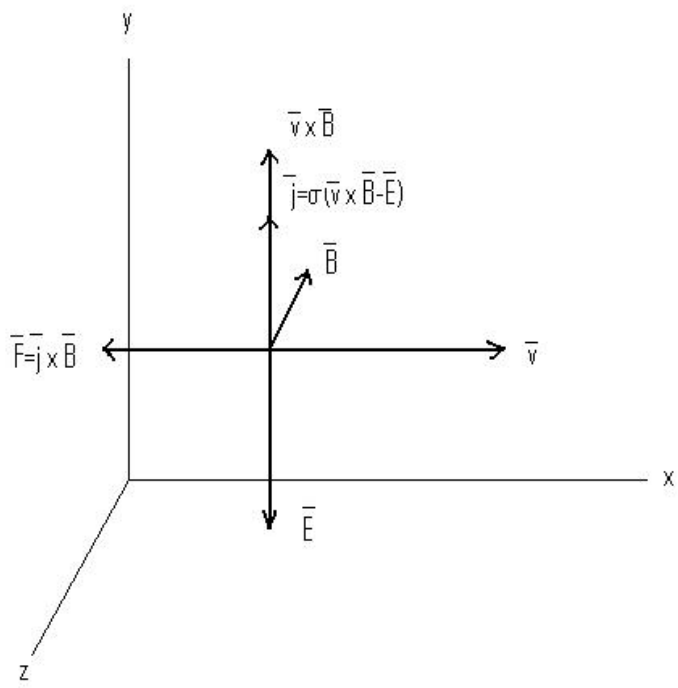


Figure 2-1. Diagram of vector components within an MHD Generator.

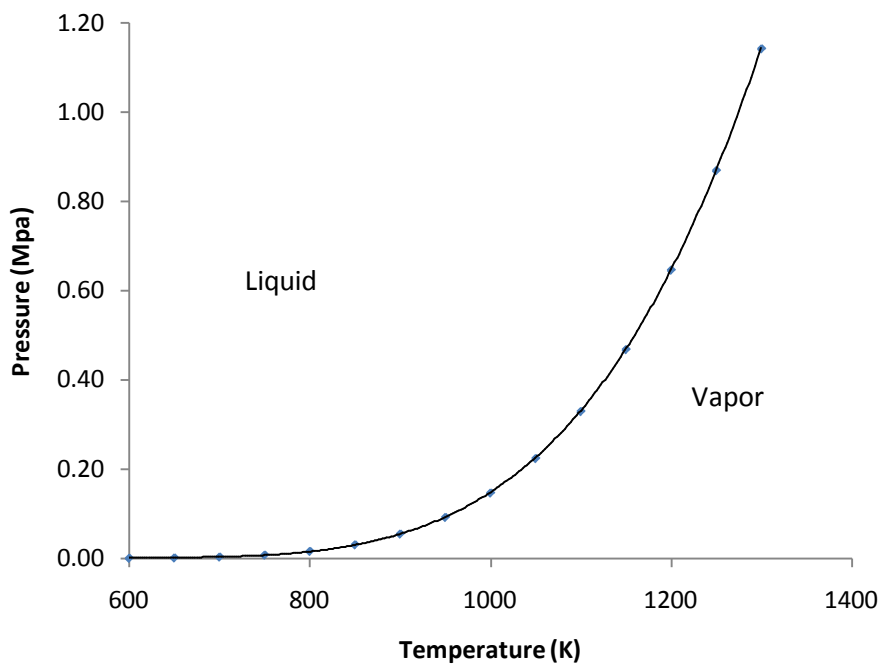


Figure 2-2. Rubidium Liquid-Vapor Saturation Curve

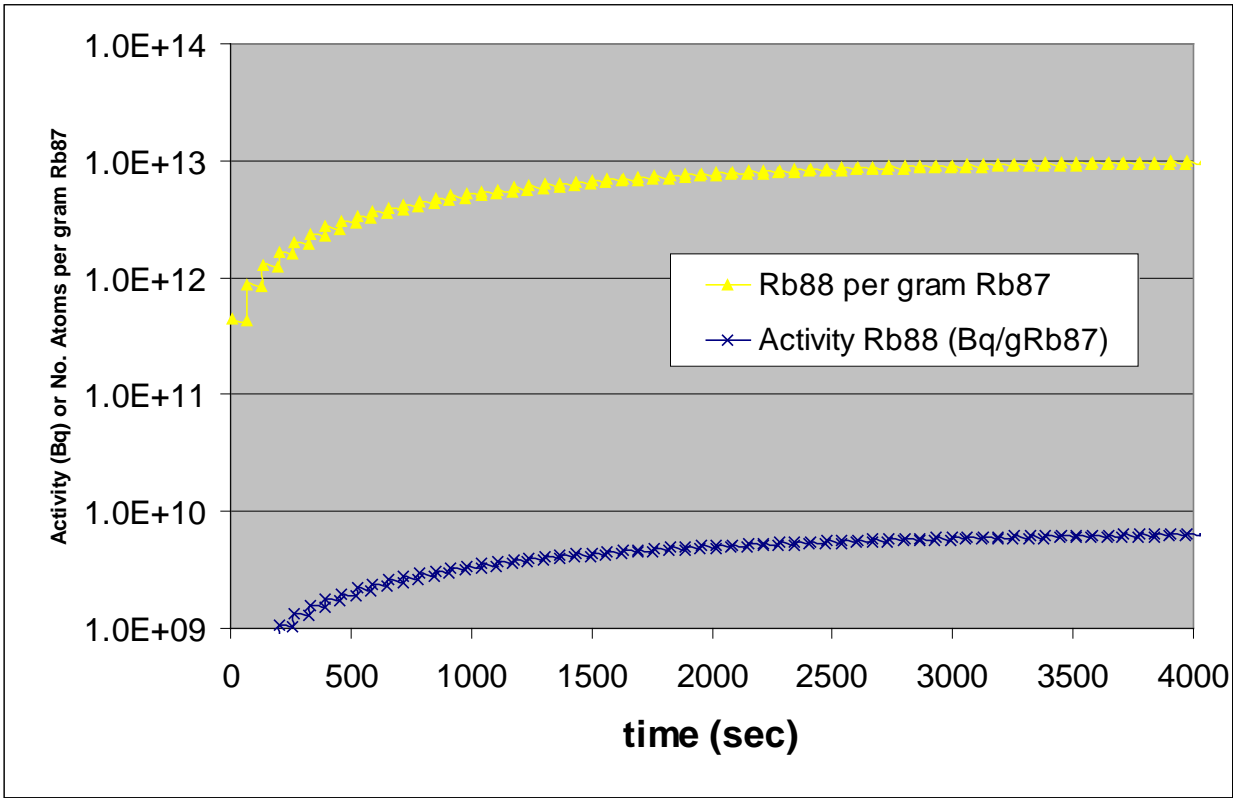


Figure 2-3. Amount of Rb-88 and Activity of Rb-88 per gram of Rubidium-87 vs. time within a closed cycle loop. (Anghaie, 2007)

## CHAPTER 3 SQUARE LATTICE HONEY COMB REACTOR

### **Reactor Description**

The Square Lattice Honey Comb (SLHC) reactor is a very compact, high power density, high temperature reactor optimized for space applications. The SLHC reactor was originally designed for nuclear thermal propulsion by the Innovative Nuclear Space Power and Propulsion Institute at the University of Florida. The reactor is fueled with solid 93% enriched uranium tri-carbide (U,Zr,Nb)C which has a melting temperature well in excess of 3000 K (Gouw, 2005).

### **Core Description**

Figure 3-1 shows the arrangement of the tri-carbide fuel within the reactor. The fuel is fabricated in the form of grooved wafers with a thickness of 2 mm. When these wafers are interlocked they form a square honey comb structure in the shape of a hockey puck 9 mm thick. The cross sectional flow area can vary depending on the total power and heat transfer characteristics desired for a particular reactor system. Several of these hockey puck-like fuel structures are stacked together and surrounded by a graphite coating inside a zirconium oxide coating to form a fuel sub assembly 45 cm long. Eighteen fuel sub assemblies are placed in two concentric circles (6 sub assemblies in the inner circle, 12 sub assemblies in the outer circle) within a zirconium hydride (ZrH<sub>2</sub>) moderator (Gouw, 2005)

### **Reflector and Control Drums**

The core is surrounded by a beryllium reflector on the top and bottom as well as radially. Control of the reactor is accomplished through six control drums that symmetrically surround the core located within the reflector. Each control drum has two sides—one composed of beryllium and the other composed of boron carbide (B<sub>4</sub>C) containing 100% boron-10. Boron-10 has a very large neutron absorption cross section and by rotating the B<sub>4</sub>C side of each control drum toward

or away from the core, the fission reaction can be controlled. Figure 3-2 shows a cross section of the entire reactor as well as dimensions for the original SLHC reactor.

### **Neutronic Modeling**

All neutronic modeling performed, with the exception of burnup studies, investigated steady state neutronics of the reactor. MCNPX version 2.6f was used to model all neutronics of the rubidium cooled square lattice honey comb reactor. MCNPX is the next generation Monte Carlo radiation transport code developed by Los Alamos National Laboratory. The code tracks virtually all radiation particles at nearly all energies. Although MCNPX is still in the development stage, it is “guaranteed to do everything MCNP5 does as well or better” (Pelowitz, 2005). What is more, MCNPX version 2.6f has the capability to calculate burnup—a capability previous versions of MCNP never had. This capability to perform burnup was the primary reason this version of MCNP was used instead of MCNP5.

The core was modeled with one-sixth symmetry using mirror-reflection boundaries on the two sides. Figure 3-3 shows the MCNP model of the original SLHC. This allows MCNP-X to generate accurate results in less time than modeling the entire reactor.

Homogenizing the fuel and rubidium coolant was also done to reduce the geometrical complexity of the model as well as computational time. The homogenizing of the fuel and rubidium coolant was done at multiple axial regions to account for the significant rubidium density changes as it changes phase through the core. This can be seen in Figure 3-4. Changes in rubidium density could have dramatic effects on the neutron reaction rates within the reactor. Since rubidium enters the core as a subcooled liquid and exits the core as a superheated vapor, the rubidium density will change by approximately three orders of magnitude between the bottom and top of the reactor. This degree of density change necessitates dividing the homogenized fuel into axial regions of different densities. Densities were calculated based off

the linear heat generation rate (LHGR) in the thermal hydraulic analysis and then updated in MCNP until convergence of both the positions and densities of the regions were achieved. Two regions were made to specifically account for the large density changes as rubidium changes phase from a liquid to a gas.

Four fuels were modeled to assess differences in burnup as well as the flux and power profiles. For each fuel 80% of the tri-carbide was zirconium. Uranium and niobium concentrations were varied to make up the remaining amount of the tri-carbide fuel. One fuel had uranium making up 5% of the tri-carbide, another used 8%, and a third had a varied concentration with the uranium concentration set to 2.5% in regions 1A and 1B and at 8% for the remaining fuel (as seen in Figure 3-4). Finally a fourth constant concentration fuel was sought to know the maximum fuel loading to achieve maximum burnup while still maintaining control of the reaction. Uranium-235 enrichment was kept at 93 atom percent for all fuels.

### **Material Cross Sections**

Based on expected fuel temperatures and cross sections available in the MCNP-X library, cross sections for uranium-235 and uranium-238 were taken from a library developed from temperatures at 1200 K. Although fuel temperatures at the exit of the core are expected to exceed 2000 K, the next highest temperature for which cross sections were available was at 3000 K. Therefore, a comparison between  $k$  effective values was performed for the two fuel temperature cross sections. All other fuel isotopes used default cross sections because appropriate temperature cross sections were not available.

The zirconium hydride and beryllium cross-sections incorporated  $S(\alpha,\beta)$  treatment for thermal neutron scattering in the moderator and reflector respectively. All other materials composing the reactor used the default cross sections.

## **K-code**

K-code is a function in MCNP that calculates the criticality,  $k$ , of the system modeled. Since this model is representative of the entire reactor, the  $k$  value calculated by MCNP represents effective criticality or  $k_{\text{eff}}$ . All K-code calculations were calculated with 1000 particles per cycle 200 skip cycles and 3200 total cycles. Any (n,2n) reactions within the beryllium are not preserved in the homogenous source term from cycle to cycle and thus only 1000 particles per cycle may not converge on the true source term and  $k_{\text{eff}}$ . Therefore, MCNP runs were done with 10,000 particles per cycle to validate that the 1000 particle per cycle runs converge on the correct  $k_{\text{eff}}$ .

## **Mesh Tallies**

Mesh tallies were used to ascertain neutron flux profiles within the fuel as well as along the boundaries of the reactor. Neutron flux tallies within the fuel were calculated for total flux, thermal flux and fast flux. Thermal neutron flux is defined as neutrons with energies between 0 and 1.86 eV and fast neutron flux with neutron energies between 1.86 and 20 MeV. Neutrons of energies above 20 MeV are very uncommon and have a negligible impact on the system. An energy deposition tally was also used in the fuel to develop axial power profiles.

## **True Fluxes and Power**

Tallies provided by MCNP are per source particle and therefore must be adjusted by reactor power to represent actual values. The total power of a reactor can be found through the following relationship.

$$Power = \int \phi(E, \vec{r}) * \Sigma_f(E, \vec{r}) dV * C \quad (3-1)$$

where  $\phi(E, r)$  represents energy and space dependent flux,  $\Sigma_f(E, r)$  represents energy and space dependent macroscopic fission cross-section, and  $C$  is the energy released per fission. The macroscopic fission cross-section is space dependent even within the fuel for the case where the

amount of fuel varies axially. For this analysis, it is assumed that each fuel sub assembly contributes equally to the total power and therefore, each fuel sub assembly makes up 1/18<sup>th</sup> of the total power. Additionally, all the power generated is assumed to be generated in the fuel, and therefore, only energy deposition and fluxes within the fuel are used. Therefore, the only space dependence used to calculate power is variation in core height, z. Since the units of the constant C are energy per fission the remaining terms make up the axial power shape and must have units of fissions per second. The axial power shape is provided by the energy mesh tally and therefore, to scale both power profile and fluxes to any power necessitates finding the new constant C' that allows normalization to a reactor thermal power. Since total reactor power is a specified quantity, the constant C' can be found by

$$C' = \frac{Power}{\sum(Emesh(z)*dz)} \quad (3-2)$$

Once the constant C' is determined the Linear Heat Generation Rate (LHGR) for a sub fuel assembly as well as any flux anywhere in the reactor can be found by Equation 3-3 and 3-4 respectively.

$$LHGR(z) = C' * Emesh(z) \quad (3-3)$$

$$\phi(z) = C' * Fluxmesh(z) \quad (3-4)$$

## **Burnup**

Burnup was done using the BURN card which is a new feature in MCNP-X. This depletion capability is a linked process between the steady state flux calculations in a KCODE run of MCNPX and a depletion code called CINDER90. KCODE calculates the systems k eigenvalue, a 63 group flux, energy integrated reaction rates, fission multiplicity, and recoverable energy per fission which are then sent to CINDER90. CINDER90 performs a depletion

calculation to determine the new number densities for burning materials which are sent back to MCNPX for another KCODE calculation at the next time step (Hendricks, 2007).

The depletion calculations use a predictor-corrector methodology. This is done by CINDER90 first performing depletion calculations for a period of half the time set. MCNPX then generates the new fluxes and collision densities at this half time step. These first two steps are known as the predictor calculation. These new fluxes and collision density allow CINDER90 to perform a corrector calculation to ascertain the number densities at the end of the time step.

The BURN capability in MCNPX performs depletion calculations only on the materials specified. Additionally, the user defines the power at which the reactor will run while undergoing burnup. The model of the SLHC in MCNP represents only one-sixth of the reactor. Therefore, the power was set to one sixth of the total reactor power. Additionally, as the burn code of MCNP progresses, each material is updated to account for the depletion of fissile materials, the buildup of fission products, and other transmutations caused by the neutron flux. If the entire fuel was composed using the same material ID, the calculations would cause the fuel to burnup equally. Since different regions of the core experience different neutron flux levels, the materials in those regions burnup at different rates. The axial fuel regions, which were developed to account for flux changes due to rubidium density changes, also allow for each region to burnup differently according to the amount of uranium in the fuel as well as the average flux exposure. This is because each fuel region has a different material ID.

### **Thermal Hydraulic Analysis**

The final MCNP model was developed over several iterations between the power profile generated from MCNP and the axial rubidium density calculations based on the previous profile. Thermal hydraulic analysis of the rubidium cooled SLHC reactor was conducted on a single channel within a sub fuel assembly. The geometry of this channel was determined based on the

sub fuel assembly size, fuel wafer thickness, and the desired cross sectional flow area. Since the rubidium coolant is contained by the fuel on all sides, closed channel analysis was performed.

The heating of rubidium inside the SLHC reactor results in a phase change from liquid to vapor. Therefore, thermal hydraulic modeling of the rubidium coolant inside the reactor must account for these two different phases as well as a transitional region where both phases exist simultaneously.

### **Two Phase Flow Effects**

This transitional region, referred to as two phase flow, requires special attention. First, the axial temperature and pressure changes through this region are much different than for either single phase. Although the coolant is still being heated from the walls of the channel, instead of increasing the coolant temperature the energy goes into the phase change from liquid to gas. This phase change consumes energy with virtually no temperature increase because the energy goes into increasing the kinetic energy of the vapor particles. This change in velocity also has an effect on pressure drop through the channel. As the speed of the coolant increases a corresponding decrease in pressure occurs. Additionally, since the phase change happens over a finite length of the core, even remotely accurate modeling must account for the temperature and pressure behavior in this region.

Two phase flow also has profound impact on a systems heat transfer characteristic. This is because liquids and gases have very different heat transfer coefficients. A coolant's ability to transfer heat is proportional to the coolant's thermal conductivity. Liquid rubidium has a thermal conductivity of 20.3 W/(m-K) at 1000 K whereas rubidium vapor has a thermal conductivity of 0.0118 W/(m-K). This three order of magnitude difference in thermal conductivity can cause drastic changes in the heat transfer coefficient and in turn the fuel temperature.

Two phase flow is generally a very complex process where flow geometry, mass flux, fluid type, and heat flux all have significant and interacting impact on the flow. Depending on the nature of these parameters, different flow regimes can occur which also drastically affect the heat transfer coefficient during the two phase portion of the flow. Flow regimes describe the manner in which the liquid and vapor exist within the geometry and are often related to void fraction. Void fraction is the fraction of volume taken up by the vapor to the total volume. Unless there are very high mass fluxes, the vapor and liquid are not usually homogeneously dispersed in the medium. For, the case of annular flow which occurs at large void fractions (greater than 0.6) the vapor exists internally while a layer of liquid film is in contact with the wall (Todreas, 1990). In this flow regime, heat transfer from the wall is dominated by the liquid and the heat transfer coefficient remains relatively high. However, once liquid contact with the wall is lost, the heat transfer coefficient will deteriorate rapidly (Kandlikar, 1999).

The critical heat flux is the heat flux at which the heat transfer coefficient diminishes drastically due to the loss of liquid contact with the wall and stagnant or relatively stagnant vapor in contact with the wall. Critical heat flux is influenced strongly by the mechanism causing loss of liquid vapor contact. For high quality two phase systems undergoing saturated boiling, critical heat flux would be reached when dryout occurs (Todreas, 1990). Dryout is the process where the annular liquid film surrounding the wall is vaporized and a film of non-flowing or very slow moving vapor exists along the wall.

### **Liquid Phase Temperature and Pressure Modeling**

The single phase liquid rubidium entering the core was treated as incompressible with an entrance temperature between 950 and 1250 K and corresponding subcooled pressures of 450 to 1000 kPa. Constant specific heat and viscosity were assumed. The axial temperature of the

rubidium coolant in the liquid phase was determined based on a predetermined linear heat generation rate (LHGR) using

$$T(z) = \int_0^z \frac{q'(z)}{\dot{m} * c_{pf}} dz \quad (3-5)$$

where  $q'(z)$  is the LHGR,  $\dot{m}$  is the mass flow rate, and  $c_{pf}$  is the specific heat of the rubidium liquid. For the first iteration, the LHGR was set to a constant based off a total core thermal power.

The pressure drop in the rubidium liquid phase only accounts for frictional affects because the fluid is assumed incompressible, and therefore, accelerational pressure drop would be negligible in a constant area channel. Gravitational pressure drop is not calculated because the system is intended for use in earth orbit. The friction factor used for calculating pressure drop was determined using the McAdams relation for a smooth tube shown in Equation 3-6. The liquid phase axial pressure distribution was calculated using Equation 3-7 (Todreas, 1990).

$$f = 0.184 * Re^{-0.2} \quad (3-6)$$

$$P(z) = \int_0^z \frac{f G^2}{2 * D_h * \rho_f} * dz \quad (3-7)$$

The liquid phase calculations were terminated when saturation conditions were met.

### **Two Phase Temperature and Pressure Modeling**

Two phase modeling of the rubidium coolant was done using the homogeneous equilibrium model (HEM). As recommended by Todreas (1990), the homogeneous equilibrium model was chosen due to the lack of a better model of boiling rubidium capable of incorporating high exit qualities, the appropriate geometry, and appropriate pressure and mass flux . The HEM makes the simplifying assumption that both the liquid and vapor phases have the same velocity. During the phase change, temperature is assumed to be constant until the quality of the rubidium

equals 1.0 and vaporization is complete. Quality was determined based on the heat of vaporization  $h_{fg}$  using Equation 3-8 from the position where boiling starts,  $z_b$ .

$$x(z) = \int_{z_b}^z \frac{q'(z)}{\dot{m} * h_{fg}} dz \quad (3-8)$$

The two phase pressure drop accounts for frictional and accelerational affects.

Accelerational pressure drop is no longer negligible because significant changes in density and therefore, velocity occur as the phase change occurs. Using the HEM, the incremental acceleration pressure drop is given by

$$\left(\frac{dp}{dz}\right)_{acc} = G^2 * \left(\frac{1}{\rho_g} - \frac{1}{\rho_f}\right) \frac{dx}{dz} \quad (3-9)$$

where  $G$  is the mass flux,  $\rho_g$  is the vapor density, and  $\rho_f$  is the liquid density (Todreas 1990).

For the frictional pressure drop, the two phase viscosity was set to the same value as at liquid saturation. This was done because the viscosity of saturated rubidium vapor was not available. Therefore, a two phase friction factor derived from a correlation of two phase viscosity could not be used. However, the frictional pressure drop does take into account the density change during the phase change. The two phase axial pressure was calculated using

$$\left(\frac{dp}{dz}\right)_{fric} = \frac{f_{lo} G^2}{2D_h \rho_f} * \left[1 + x \left(\frac{\rho_f}{\rho_g} - 1\right)\right]. \quad (3-10)$$

The two phase calculations were terminated after complete vaporization ( $x=1.0$ ).

### **Vapor Phase Temperature and Pressure**

The axial temperature distribution of the rubidium vapor was calculated using Equation 3-5 but using the specific heat for the vapor at each particular state as it is heated. A vapor specific heat is no longer constant and varies with changes in temperature and pressure.

Additionally, vapor viscosity data was not available above 500 kPa or above 1500 K. Therefore,

estimates for vapor viscosity were based off a linear temperature relationship of the viscosity data at 500 kPa.

The pressure drop in the single phase rubidium vapor portion of the core accounts for only frictional affects and was calculated with Equations 3-6 and 3-7 using property data for rubidium vapor.

### **Heat Transfer Coefficients**

The liquid phase rubidium heat transfer was calculated using two different correlations. According to Carbajo (2005), the Lubarsky & Kaufman correlation compares well with heat transfer experiments done with other liquid alkali metals. The Lubarsky and Kaufman equation is

$$\frac{hD}{k} = 0.625 \left( \frac{DGc_p}{k} \right)^{0.4} . \quad (3-11)$$

Whitte's correlation, which was developed from data of forced convection from a sphere to liquid sodium, was also used (Stavros et al., 2001).

$$\frac{hD}{k} = 2 + 0.386(Re * Pr)^{0.5} . \quad (3-12)$$

The heat transfer coefficient for rubidium vapor was based on the empirical formula for forced convection from a sphere (Bird, et al., 1960).

$$\frac{hD}{k_g} = 2 + 0.6Re_g^{1/2} Pr^{1/3} \quad (3-13)$$

### **Critical Heat Flux**

The heat transfer coefficient in the two phase region depends largely on whether the critical heat flux is reached. If it is reached the heat transfer coefficient is likely to be smaller than the single phase vapor coefficient at the same pressure and temperature. If critical heat flux is not achieved, the heat transfer coefficient is likely to transition with void fraction relatively

smoothly from the liquid phase heat transfer coefficient to the vapor phase heat transfer coefficient.

Like other two phase flow phenomenon, there is not a single analytical relationship for critical heat flux that applies to all geometries, flow rates, fluids and other system parameters. Therefore, critical heat flux is usually found using the most appropriate model. Two phase models for rubidium could not be found. Since rubidium is an alkali metal, it is assumed that it would behave similarly to other alkali metals in a heated two phase flow. Therefore, a critical heat flux relationship for another alkali metal is assumed to be reasonably accurate. According to Tong and Tang (1997), results of dryout critical heat flux experiments on boiling potassium were found to agree well with a CHF correlation developed for water by Lowdermilk. This correlation is assumed to work well for other alkali metals including rubidium.

$$q''_{crit} = 270D^{-0.2}(L/D)^{-0.85}G^{0.85} \quad (3-14)$$

$$\text{For } G/(L/D)^2 < 150$$

$$q''_{crit} = 1400D^{-0.2}(L/D)^{-0.15}G^{0.5} \quad (3-15)$$

$$\text{For } G/(L/D)^2 > 150$$

### **Fuel Temperature**

Tri-carbide fuels were originally developed by the Rover/NERVA program from 1955 to 1973. These fuels have melting temperatures around 3800 K and thermal conductivity between 30 and 70 W/(m-K). Although more test data was needed, at the conclusion of Rover/NERVA tri-carbide fuel was expected to be operated at temperatures of 3000 K without problems (Anghaie and Knight, 2004). Therefore, 3000 K represents the maximum allowed fuel temperature for this design. Also, to perform a conservative estimate of centerline fuel temperature, a fuel thermal conductivity of 30 W/(m-K) was used.

Heat transfer in the fuel was simplified as to represent a 1-D slab of the same total volume and thickness where heat generated at any axial position is transferred laterally in one dimension to the rubidium coolant. Figure 3-5 shows a depiction of the simplified model as compared to the actual geometry. The 1-D model predicts the same centerline fuel temperature along the entire centerline at any set axial position. However, because the real geometry has corners, the same amount of fuel shares less convective surface area. This fact will cause the highest temperatures in the fuel to occur along the centerline of these corners.

In addition to the 1-D model developed, Heating 7.3 was used to more accurately predict fuel temperatures. The Heating 7.3 model represents one quarter of the actual coolant channel and does not model rubidium and can be seen in Figure 3-5. All sides of the fuel with the exception of where the fuel would be in contact with the rubidium coolant were modeled as reflective boundary conditions. The fuel surface in contact with rubidium was provided with a forced convection boundary condition that corresponded to the same axial rubidium temperatures and heat transfer coefficients ascertained from the thermal hydraulic model. Axial variation in volumetric heating within the fuel was also changed to match the power profile of any fuel type.

### **Reactor Mass Estimate**

Mass of the reactor includes all the materials in the MCNP model. This includes the fuel, moderator, control drums and axial and radial reflectors. The mass of each reactor component was calculated by multiplying the volume of each material by its number density. Due to the very high density of boron carbide, the size of the control drums can potentially influence the mass of the reactor by a very large amount. Therefore, the neutron absorbing portions of the control drums must be large enough to effectively control the reactor and yet still small enough to limit the reactor mass.

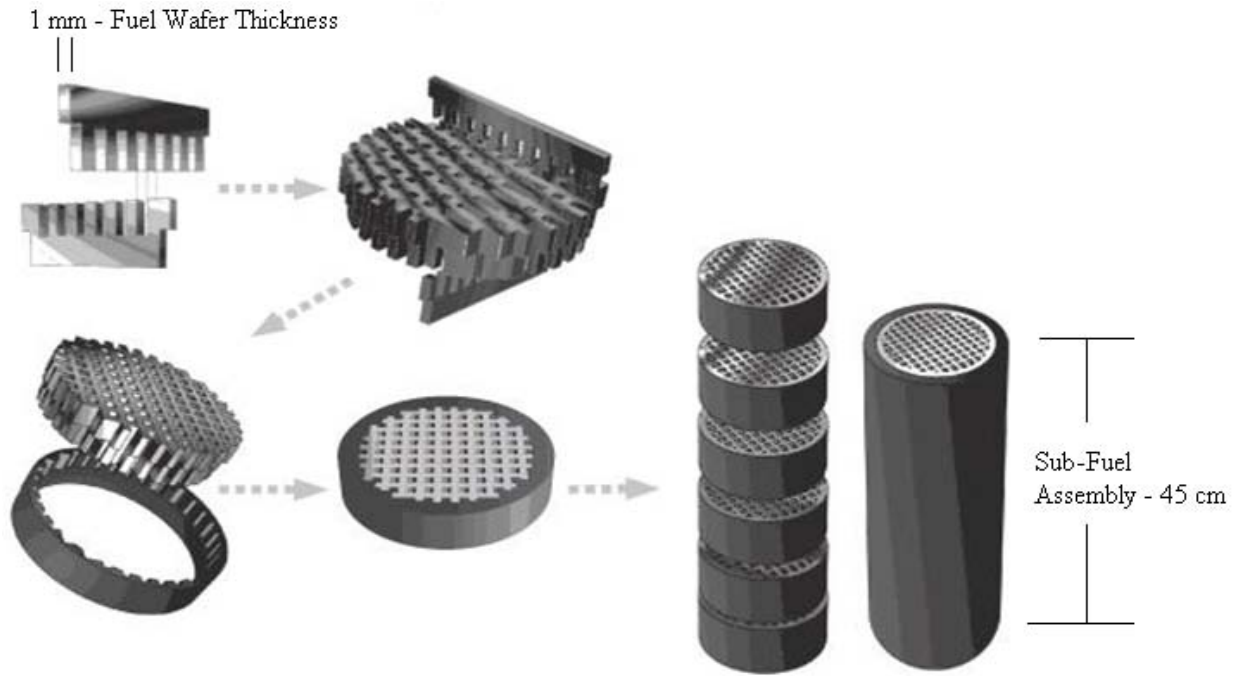


Figure 3-1. Arrangement of tri-carbide fuel to form a fuel sub assembly in the SLHC reactor.

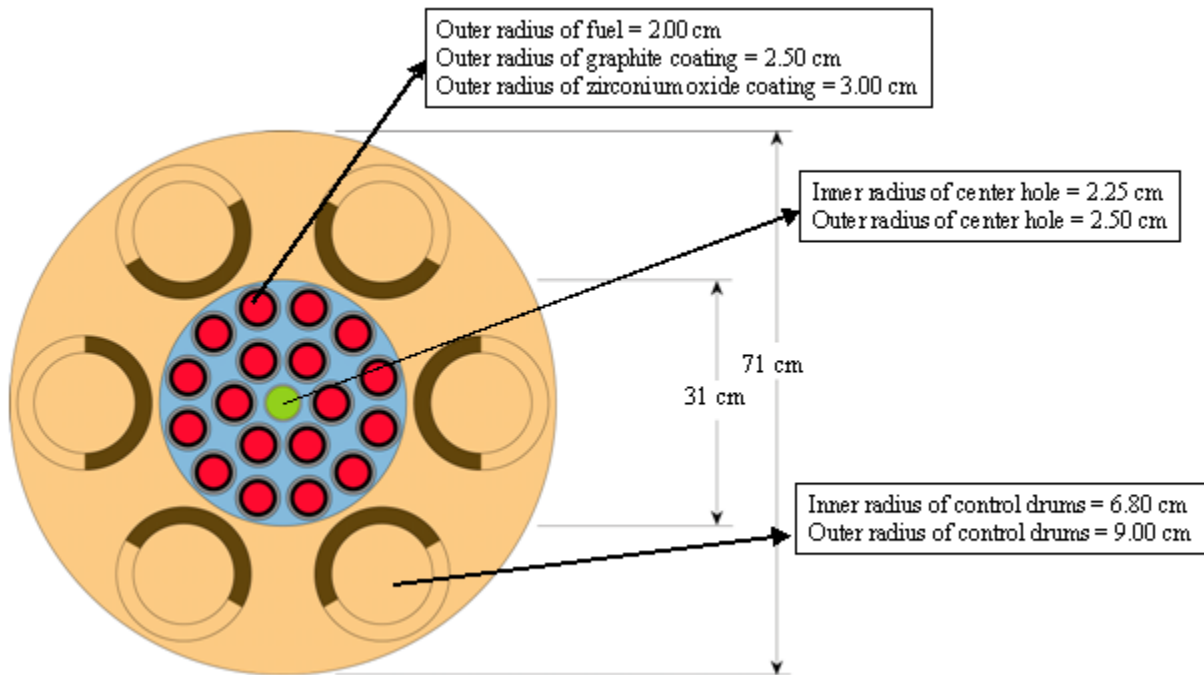


Figure 3-2. Cross-sectional view of original SLHC reactor

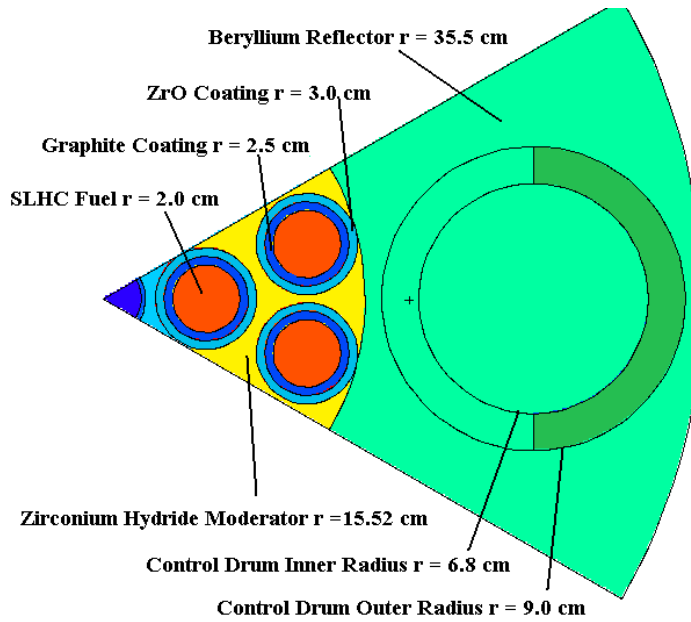


Figure 3-3. 1/Sixth MCNP model of SLHC reactor

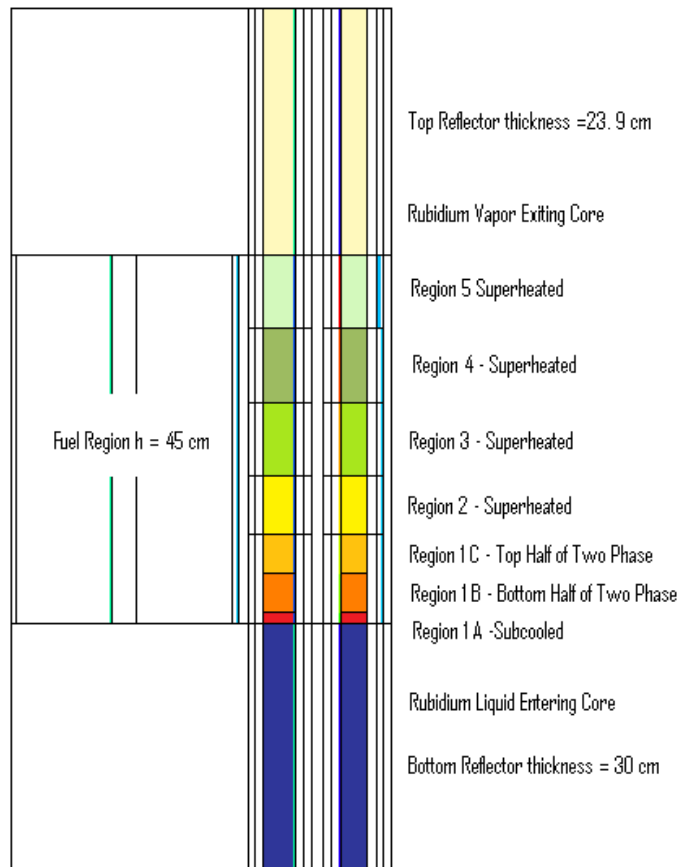


Figure 3-4. Axial view of SLHC reactor depicting fuel regions based on changes in rubidium density

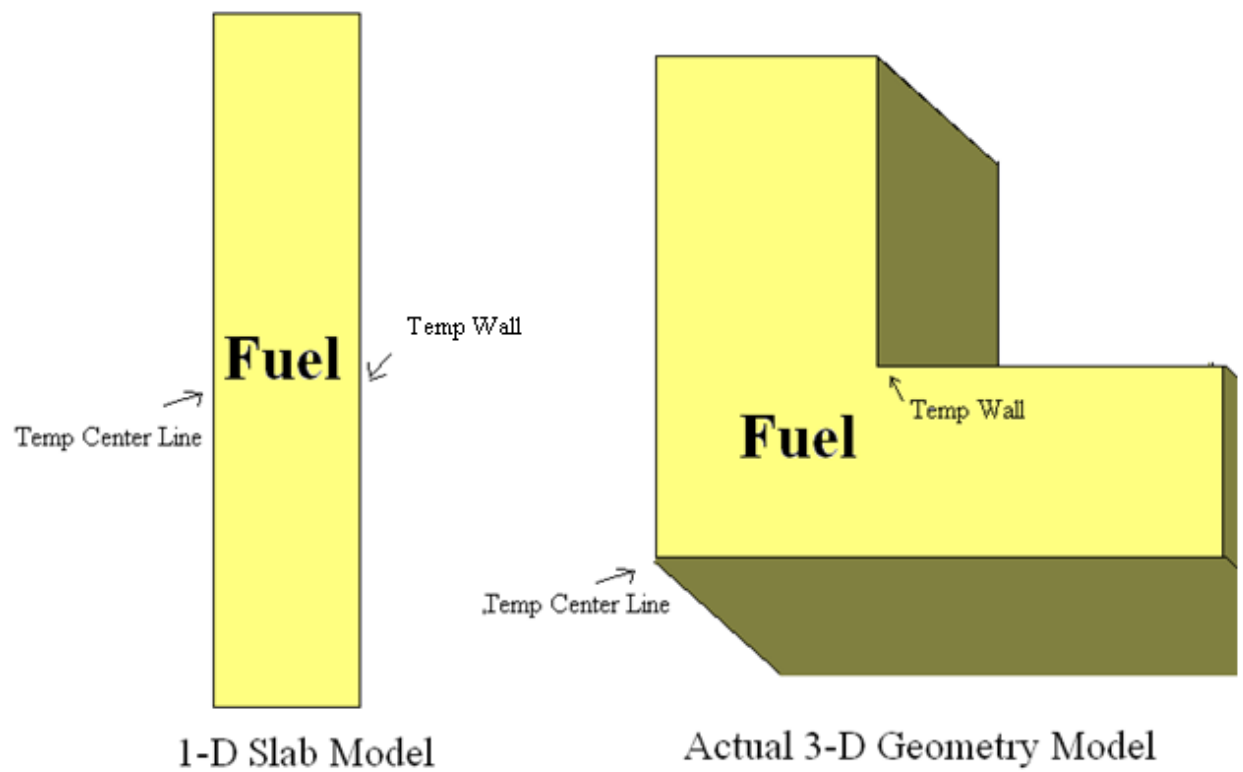


Figure 3-5. Visual depiction of the fuel heat transfer models.

CHAPTER 4  
OTHER SPACECRAFT COMPONENTS

**Nozzle and Diffuser**

**Thermal Hydraulic Modeling**

The nozzle serves the purpose of accelerating flow after it exits the core into the MHD generator. The diffuser serves a similar but opposite function of slowing down the rubidium flow after it exits the MHD generator so that the flow is at a slow speed upon entering the condenser. The nozzle (if needed since in some conditions the flow exits the core at Mach=0.7) and diffuser were modeled as isentropic systems. An isentropic process assumes no losses so that the vapor's total temperature and total pressure remain constant. For an ideal gas, the expression for total temperature and total pressure ratios are as follows.

$$\frac{T_t}{T} = 1 + \frac{\gamma-1}{2} M^2 \quad (4-1)$$

$$\frac{P_t}{P} = \left(\frac{T_t}{T}\right)^{\gamma/(\gamma-1)} \quad (4-2)$$

Combined with the continuity equation the exit area and exit properties of the fluid can be found for both the nozzle and diffuser. The amount of expansion or compression can be limited by a desired exit Mach number. For the diffuser, an exit Mach number of 0.2 was adequate for condenser entrance.

**Mass Estimate**

Nozzle and diffuser masses were estimated based off previous work done by Anghaie, (2000) and Maya et al (1993). They found that the specific masses for nozzles and diffusers were 0.004 kg/kWe and 0.006 kg/kWe respectively. Since these specific masses are very small it is expected that the nozzle and diffuser will contribute very little to the total system mass.

## Condensing Radiator

Advanced radiator concepts for space applications have been studied extensively in the last 20 years. One promising design is that originally proposed by Begg and Engdahl (1989) which consists of a cylindrical radiator composed of potassium heat pipes of SiC reinforced Ti with carbon graphite composite fins. As seen in Figure 4-1, the flow is divided into multiple channels which pass on the inside of the cylindrical radiator. As the rubidium flows through these channels the tiny potassium heat pipes remove heat from the rubidium to the carbon graphite fins. The fins then radiate the heat into space.

### Thermal Hydraulic Modeling

The condenser was modeled as a series of cylindrical flow channels with a diameter of 1 mm and each separated by 0.5 mm of radiator to form the cylindrical radiator. The total flow area was kept the same as the exit area of the diffuser, and the external surface of the condenser was assumed to be the same temperature as the rubidium coolant inside. The temperature in space is only 2.725 K and can be assumed zero since the temperature of the graphite is much higher. Therefore, the heat flux removed from the rubidium was given by

$$q'' = \varepsilon\sigma_{SB}T^4 \quad (4-3)$$

where  $\varepsilon$  is the graphites emissivity and  $\sigma_{SB}$  is the Stephan-Boltzmann constant. The carbon graphite has been found to have an emissivity greater than 0.85 for the range of wavelengths 0.5 to 4  $\mu\text{m}$  (725 to 5796 K) according to Neuer (1995). Therefore, an emissivity of 0.85 was used.

The condenser was modeled to condense the rubidium vapor until it was saturated liquid. Pressure changes were calculated in the same manner as within the core using the HEM model for the two phase flow portion.

## Mass Estimate

Based on a heat rejection temperature of 875 K, the reference radiator design by Begg and Engdahl (1989) achieved a specific mass of 6.5 kg/m<sup>2</sup> (Begg & Engdahl, 1989). Since the rubidium heat rejection temperature is between 1000 and 1300 K, the specific mass of the radiator was increased by a factor of 2.3 to use a heat pipe material such as molybdenum alloy which can take higher stresses at these high temperatures. Therefore, the condenser mass estimate was the product of the total condenser area calculated in the thermal hydraulic analysis and 14.95 kg/m<sup>2</sup>.

## Pump

### Thermohydraulic Modeling

Rubidium was condensed to a liquid because it is very inefficient to pump a gas. This is because the pumping power is inversely proportional to the fluid's density as seen in Equation 4-5. The exit pressure was set to the initial core entrance pressure and the exit temperature was calculated based off the change in enthalpy. Liquid metal pumps can generally achieve efficiencies of 90 percent or higher but to keep this analysis conservative a pump efficiency of 0.75 was used.

$$dh = \frac{P_2 - P_1}{\rho\eta} \quad (4-5)$$

### Mass Estimate

Work done by Maya et al (1993) included a survey of centrifugal pump systems to determine the average pump mass. The recorded mass of each pumping system in the survey was actually the shipping mass which provides a more conservative figure since there are often additional components included with shipping that are not present in the installation. This

survey concluded an average of 9.3 kg per kW of pumping power and was used to estimate the mass of the pump in this system

### **Power Management and Distribution System**

The Power Management and Distribution (PMAD) system includes the control systems for managing the power created in the MHD generator and operating the magnetoplasmadynamic (MPD) thruster as well as the thruster itself. MPD thrusters produce about 100 kg of thrust per megawatt of electrical power and have specific impulses between 4000-10000 s<sup>-1</sup> (NASA Glenn Research Center, 2008). The mass of the PMAD system was also estimated from previous work that used a modified version of the PMAD code developed by Metcalf (1993) that allowed for variation in MHD power as well as thruster type. The PMAD mass includes the mass of the pulse power unit (PPU) including the radiator for a pulsed plasma thruster, transmission lines, and load switch gear with radiator. For the magnetoplasmadynamic thruster a specific mass of 1.24 kg/kWe was found for the PMAD from that study.

### **Radiation Shield**

Although this spacecraft is unmanned, shielding remains an essential component of the spacecraft. This is because many components on the spacecraft will degrade and not function if they are exposed to high levels of radiation. Therefore a shield serves to protect sensitive components of the spacecraft from the high radiation fluxes exiting the reactor.

### **Radiation Damage Limits**

The two main sources of radiation exiting the reactor are neutrons and gamma rays. The book by Angelo and Buden (1985) shows the typical radiation damage thresholds for many components often found on spacecraft. Different components have different radiation damage thresholds. The most sensitive systems such as the spacecraft computers and guidance control can receive a lifetime neutron dose of 10<sup>11</sup> n/cm<sup>2</sup> and a gamma dose of 10<sup>5</sup> rad. The vast

majority of remaining system components can receive a dose of one order of magnitude higher or more. The amount of exposure components receive is related to the gamma and neutron flux exiting the reactor, the amount and type of shielding, and the distance the component is from the shield. The most sensitive equipment must be placed the furthest from the shield.

### **Shadow Shield**

A shadow shield provides the best protection with the least amount of mass. Instead of shielding the entire reactor a shadow shield shields one side of the reactor and casts a shadow of protection in that direction from the reactor. Figure 4-2 illustrates the concept of the shadow shield. Since the vast amount of radiation is generated in the core the protective shield can be thought to generate a shadow cone by the angle generated between the outside of the top of the core and the outside of the shield. Therefore, as the distance behind the shield increases the protected area increases as well.

### **Neutron shielding**

Hydrogen containing materials make the most effective neutron attenuating materials. This is because hydrogen is the most effective element at scattering neutrons. This is the primary reason why most moderating material used in reactors contain hydrogen such as water. Liquid hydrogen used as the propellant for the MPD thrusters can serve as part of the shield, however, the amount of shield decreases with fuel consumption. Lithium hydride (LiH) is generally considered the best shielding material because of its large hydrogen number density ( $N_H=5.9E+22$  atoms/cm<sup>3</sup>) and low mass density (0.775 g/cm<sup>3</sup>) (Angelo and Buden, 1985).

### **Gamma shielding**

While LiH does provide some shielding from gamma rays, high atomic number materials serve as better gamma ray shields. Additionally, secondary gamma rays are created from neutron interactions in the neutron shield and generally require an additional shield of high

atomic number to provide ample attenuation. Lead is generally considered among the best gamma ray shielding materials per unit mass with a density of 11.34 g/cm (Angelo and Buden, 1985).

### **Shield Modeling and Mass Estimate**

MCNPX was used to model the shadow shield below the reactor. Adjacent to the bottom axial reflector a LiH shield of equal radius followed by a lead shield was modeled. Both neutron importance and photon importance must be increased as particles penetrate further into the shield in order to get acceptable statistics. Thickness of both the LiH and lead shield will be adjusted to allow a 5 year exposure lifetime for incentive ( $10^{12}$  n/cm<sup>2</sup> and  $10^6$  rad) equipment immediately behind the shield and sensitive equipment ( $10^{11}$  n/cm<sup>2</sup> and  $10^5$  rad) equipment a distance of ten meters away from the shield. Mass estimates for the shield will be determined based of the two shield volumes and the corresponding material density.

### **Supporting Structure**

The supporting structure includes the rest of the mass of the spacecraft system power plant. The power plant does not include the hydrogen fuel tanks which serve as the propellant for the magnetoplasmadynamic thruster. The supporting structure includes all structural supports between different system components that hold the spacecraft together. It also includes the total weight of the rubidium coolant not accounted for elsewhere in this analysis. According to Angelo and Buden (1985), it is often standard practice to assume 10% of the total “dry” spacecraft mass is supporting structure.

### **Propellant and Orbital Mechanics Model**

All previously discussed components make up the dry mass of the spacecraft—the mass of the spacecraft without fuel. The amount of propellant needed for the spacecraft depends on the rate of fuel usage, the time over which the fuel is used, and the mass of the spacecraft. Since these

three factors are all interdependent and also depend on the mission of the spacecraft, an orbital mechanics model was developed to compute the fuel usage as well as other parameters of the spacecraft performing LEO to GEO transport operations.

All calculations were based off equations found in the book by Bate, Mueller, and White (1971). The model assumes that the only two accelerational forces acting on the spacecraft are the effect of earth's gravity and the thrust from the MPD thruster. The direction and magnitude of the acceleration caused by gravity is given by

$$\bar{a}_g = -\frac{GM_E}{|\bar{r}|^3} \bar{r} \quad (4-6)$$

where G is the gravitational constant  $6.673\text{E-}11 \text{ m}^3\text{kg}^{-1}\text{s}^{-2}$ ,  $M_E$  is the mass of earth, and  $\bar{r}$  is the position vector of the spacecraft with respect to the center of the earth.

Since the spacecraft electrical power is approximately 1 MW the corresponding thrust level for an MPD thruster is about 100 N. Thrust is always in the same direction as the current velocity of the spacecraft and therefore, the acceleration due to thrust is given by

$$\bar{a}_t = \frac{T}{m_s} \frac{\bar{V}}{|\bar{V}|} \quad (4-7)$$

where T is the thrust,  $m_s$  is the mass of the spacecraft, fuel, and payload when outbound, and  $\bar{V}$  is the vector velocity of the spacecraft. The total acceleration of the spacecraft is the summation of the acceleration due to gravity and the acceleration due to thrust. Over a small time interval the velocity of the spacecraft changes by the following relationship

$$\bar{V}_f = \bar{V}_i + (\bar{a}_t + \bar{a}_g)dt \quad (4-8)$$

It then follows that the position vector of the satellite changes over the same small interval by

$$\bar{R}_f = \bar{R}_i + \bar{V}_i dt \quad (4-9)$$

The model assumes the spacecraft starts at LEO at an altitude of 1000 km and ferries an average GSO satellite mass of 4500 kg to GSO orbit at an altitude 36,000 km and then returns

without the satellite mass. Fuel consumption rate is related to the MPD thruster's specific impulse by the following relationship

$$\dot{m}_f = \frac{T}{g_0 I_{sp}} \quad (4-10)$$

where  $g_0$  is the acceleration due to earth's gravity on the earth's surface (9.81 m/s<sup>2</sup>) and  $I_{sp}$  is the engines specific impulse. For fuel mass estimates a specific impulse of 10,000 s which represents the high end performance capabilities of MPD thrusters.

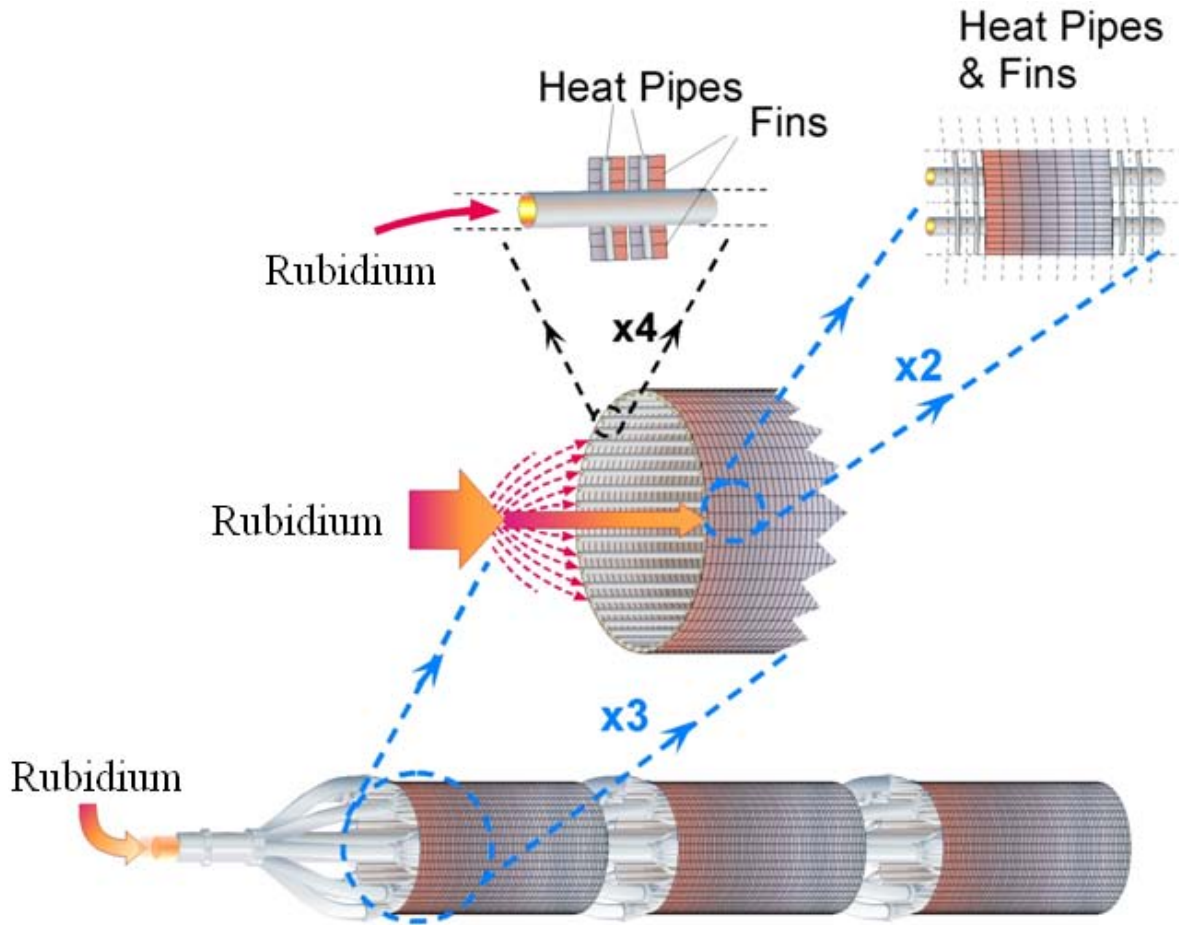


Figure 4-1. High temperature low mass radiating condenser design

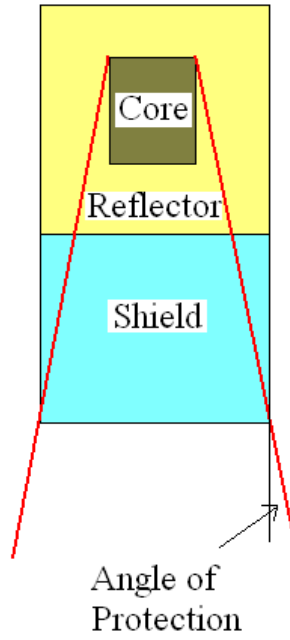


Figure 4-2. Angular protection provided by a shadow shield

## CHAPTER 5 RESULTS AND FINAL SPACECRAFT DESIGN

### **MHD Power**

The flow properties of the rubidium vapor entering the MHD determine the power generated in the MHD generator. However these properties are also constrained by reactor limits both in temperature and exit velocity. Based on preliminary heat transfer characteristics rubidium temperatures in excess of 2200 K would likely cause fuel temperatures to exceed the maximum allowable fuel temperature of 3000 K. Additionally, to avoid choked flow within the reactor exit flow speeds were not to exceed 0.7 Mach.

### **Effect of Core Exit Temperature**

Figure 5-1 shows the effect of varying temperature on both core exit Mach number and MHD power. The graph shows that both core exit Mach number and MHD power increase with increasing rubidium temperature. The increase in Mach number is small compared to the large change in electrical power over this temperature range suggesting that high temperatures are not the dominant property effecting core exit Mach number. Also, although the increase in power with increasing temperature is significant the desired electrical power of 1 MWe cannot be achieved without exceeding thermal limits of the reactor for the original design

### **Effect of Core Exit Pressure**

The effect of varying core exit pressure on both core exit Mach number and MHD power is displayed in Figure 5-2. Increasing pressure for the same entrance temperature and flow rate has the opposite effect of increasing temperature. Increasing pressure results in a dramatic decrease in core exit Mach number with a rather mild change in electrical power. The decrease in electrical power is not the result of slower flow within the MHD generator but is due to condensation occurring at a much higher temperatures when at higher pressures. Additionally,

Figure 5-2 shows the effect of expanding the flow through the isentropic nozzle to increase the velocity of the gas to Mach 1.0. Electrical power decreases with nozzle expansion because the expansion in the nozzle reduces the temperature of rubidium and less energy extraction in the MHD generator can occur prior to condensation.

### **Effect of Mass Flow Rate**

Finally the effect of varying mass flow rate on both core exit Mach number and MHD power is shown in Figure 5-3. Both core exit Mach number and electrical power increase dramatically with increasing flow rate. Results in Figure 5-3 suggest that the desired power could be achieved if flow rates of 15 kg/s or higher could be passed through the core. However, the same figure shows that Mach numbers within the core for the original design would need to exceed Mach 2. If the core exit pressure was increased to as high as 1000 kPa the Mach number would be under 1 but the electrical power would still be only half of the desired value.

The results of varying temperature, pressure, and mass flow rate indicate that temperature must be as high as possible without exceeding thermal limits for the reactor, the pressure must be as low as possible without choking in order to reduce the condensation temperature, and the mass flow rate must be sufficiently high to produce the desired electrical power. Overall this amounts to a core exit temperature around 2000 K, an exit pressure of 300 kPa and a flow rate of 15 kg/s.

### **Flow Area Design Change**

In order to accommodate the larger flow rates necessary to achieve the desired electrical power the flow area within the core must be increased. There are two means by which the flow area in the SLHC reactor could be increased. The first is to increase the percent of flow area within the fuel. The advantage of this flow increasing method is that no large scale design changes to the reactor must be made. It also improves the heat transfer characteristics of the

reactor. However an increase in flow area demands a decrease in reactor fuel. Significant changes in reactor fuel will drastically reduce the lifetime of the reactor.

The other method to increase the flow area within the reactor is to increase the size of the fuel. Increasing the fuel necessitates increasing the dimensions of the entire reactor. This not only increases spacecraft mass but it also can have significant effects on the neutronics of the reactor. However, increasing the size of the fuel not only allows for much larger increases in flow area but it also increases the amount of fuel and in turn the reactor lifetime.

The flow area necessary for a 15 kg/s flow rate without exceeding Mach 0.7 demands an increase of 360 percent. Therefore, changing the percent flow area alone cannot provide sufficient flow area. Therefore, an increase in reactor size was necessary. To accommodate the advantages of both methods, the reactor was increased radially by a factor of 1.5 and the amount of flow area was increased to 50 percent of the total area of the sub fuel assembly. This amounts to a flow area increase of 375 percent over the original design. The increased flow area results in the core exit Mach number and powers for varying flow rates shown in Figure 5-4. The figure shows that a power of nearly 1 MWe is attainable with this increased flow area.

### **Core Thermal Hydraulic Results**

In order to create the exit conditions desired for the MHD generator a reactor thermal power of 6 MW was necessary. These exit conditions are the product of the previously discussed two phase flow model with a constant linear heat generation rate (LHGR). For the scaled reactor with 50 percent flow area and a fuel wafer thickness of 2 mm the corresponding single channel constant LHGR for a 6MW reactor is 12.215 kW/m.

### **Excessive Fuel Temperature**

The axial rubidium and fuel temperatures for the scaled reactor with 2 mm thick wafer fuel can be seen in Figure 5-5. As expected the heat transfer coefficient deteriorates during the

two phase transition as seen by a significantly larger difference between rubidium temperatures and fuel temperatures. In the liquid phase, the more conservative heat transfer coefficient was from the Lubarsky and Kauffman correlation and is estimated to be  $12,504 \text{ W}/(\text{m}^2\text{-K})$ . At the core exit where both fuel and rubidium temperatures are highest, the heat transfer coefficient is estimated to be  $310 \text{ W}/(\text{m}^2\text{-K})$ . This results in fuel temperatures over 4000 K, which are not only much higher than the allowable fuel temperature but also above the absolute melting temperature of uranium tri-carbide (3800 K). Additionally, as seen in Figure 5-5, centerline temperatures are generally only a few degrees above the fuel surface temperature due to the high thermal conductivity.

### **Heat Transfer Design Change**

Fuel temperatures must be reduced below 3000 K for the reactor to operate without damage for long durations. In order to reduce temperatures, either the vapor heat transfer coefficient must be increased or the LHGR must be reduced. The vapor heat transfer coefficient, with the exception of hydraulic diameter, is a function of the properties of the fluid. Since these same properties are desired for the MHD electrical power conversion, changing them to reduce the heat transfer coefficient would be counterproductive.

The linear heat generation rate is a product of total thermal power and the number of channels within each fuel sub assembly. The thermal power of 6 MW is necessary to achieve the temperatures desired in the MHD generator. The number channels within a fuel sub assembly is a function of the fuel wafer thickness and percent flow area. With the original fuel wafer thickness of 2 mm and 50 percent flow area, the number of channels within a fuel assembly was 61. In order to increase the number of sub channels and thereby reduce the LHGR, the fuel wafer thickness was decreased to 1 mm. Keeping the percent flow area the same the number of channels was increased to 243 and the LHGR per channel dropped to 3.05 kW/m. Decreasing

the fuel wafer thickness also increased the vapor heat transfer coefficient to  $442 \text{ W}/(\text{m}^2\text{-K})$ , because the hydraulic diameter was decreased.

Figure 5-6 shows the rubidium and fuel temperatures for the 6 MW reactor with fuel wafer thickness of 1 mm for a constant linear heat generation rate (LHGR) with the 1-D model and the Heating 7.3 model, as well as LHGR for the 13 percent fuel loading with the 1-D model. The fuel centerline temperature at the exit is now 2728 K for the constant LHGR 1-D model, which is below the maximum allowable fuel temperature.

Model calculation of fuel temperatures assumed 1-D slab geometry, which overestimates the maximum temperatures. In reality, there is three dimensional heat transfer which results in peak temperatures occurring at the perpendicular intersection of the fuel wafers. Heating 7.3 predicts temperatures not to exceed 2583, based on the same axial variation in heat transfer coefficient and fuel thermal conductivity. Although it would seem that due to these intersections, the maximum fuel temperature would be greater than in the slab geometry model, due to the ability of the fuel to transfer heat within itself, temperatures at the exit are lower. In turn temperatures near the bottom are higher than predicted by the slab geometry model because these are the colder locations the heat generated at the top is transferred to. Figure 5-6 shows how this variation in maximum fuel temperature for a constant LHGR using Heating 7.3 compares to the maximum fuel temperature using the 1-D model.

Critical Heat flux was never reached for the 1 mm thick fuel wafer design. Therefore, the heat transfer coefficient is expected to gradually change from the liquid phase heat transfer coefficient to that of the vapor phase as the void fraction changes.

### **Reactor Neutronic Results**

Figure 5-7 shows the radially-increased MCNP model with dimensions. All material number densities and fractional isotope amounts can be seen in Appendix A.

## Fuel Loading and Criticality

Table 5-1 shows the  $k$  effective values for the three previously specified fuels with the control drums out and in and with the addition of a center boron carbide tube. Additionally, Table 5-1 shows the  $k_{\text{eff}}$  values for a fuel loading of 13% uranium, which represents the maximum allowed uranium concentration. All four fuel loadings indicate the core would have sufficient excess reactivity at beginning of life. The combination of increasing the amount of uranium in the fuel and radially increasing the reactor drastically limits the effectiveness of the control drums within the reflector. Therefore, for the varied, 8% and 13% fuels, a boron carbide tube in the center of the reactor can be added to keep the reactor subcritical at BOL. The effect of changing the uranium cross sections to correspond to 1200 K or 3000 K was small. The  $k$  effective values for the 13% fuel with the 1200 K and 3000 K cross sections were 1.26803 +/- 0.00047 and 1.26238 +/- 0.00046 respectively. Since the change is small, all remaining neutronic modeling used a uranium cross sections at 1200 K.

## Flux Profiles

Thermal neutron flux (0 to 1.86 eV) and total neutron flux profiles within the fuel are displayed in Figures 5-8 and 5-9 respectively. Neutron flux levels have been calculated for a core thermal power of 6 MW. The thermal profiles vary significantly for each fuel type, but all show a dramatic surge in thermal flux at the very bottom of the reactor. The surge in thermal flux at the bottom is due to the high density liquid rubidium as it enters the fuel in combination with the beryllium reflector at the bottom of the core. The smaller surge at the top is also due to the reflector but is not as high due to the lower density of rubidium vapor.

The total fluxes for all three constant concentration fuels at 6 MWth have similar shapes with peak values halfway up the core. The peak for the varied concentration fuel is shifted further up the core due to the higher concentration of uranium in the top of the reactor. The

highest total flux is for the varied percent uranium concentration at  $4.33 * 10^{14}$  n/(cm<sup>2</sup>-s). The lowest peak total flux is for the 13 percent uranium concentration at  $4.02 * 10^{14}$  n/(cm<sup>2</sup>-s).

Figure 5-8 and 5-9 show that both thermal flux and total flux decrease with increasing uranium concentration. This is expected because increasing the uranium concentration requires less neutron flux to cause the same number of fissions.

### **Linear Heat Generation Rate**

The thermal flux accounts for approximately 86% of the fission occurring in the core and therefore, the power profile based on the energy deposition tally has a very similar shape. The normalized linear heat generation rate for each type of fuel can be seen in Figure 5-10. The large spike at the bottom of the reactor increases with increased uranium concentration. Reducing the amount of uranium in the bottom of the reactor as in the varied fuel does reduce the power spike at the bottom. Additionally, although large differences in axial power factor are undesired, thermal hydraulic issues associated with this spike are not a problem because the heat transfer associated with liquid rubidium is more than adequate to prevent excessive fuel temperatures.

### **Burnup**

Operation of this system is intended to need full power for only a few days as it transports satellites from one orbit to another. The remainder of the time, the reactor operates at a very low power or uses decay heat alone to keep the rubidium sufficiently heated to remain a liquid. Based on the burnup shown in Figure 5-11, a transport vehicle with 5 % fuel loading could operate at full power for only 400 days (1.1 years). The eight percent fuel loading has a core lifetime nearly twice that at 800 days (2.2 years). This burnup could result in spacecraft lifetimes of a few years if the spacecraft is only needed at full power for a fraction of the time. However, if near continuous full power operation is needed or to increase fractional power usage lifetimes to nearly 10 years, a fuel loading of 13% is needed. This fuel loading has a burnup of

approximately 2000 days, corresponding to a continuous full power operating lifetime of 5.5 years.

### **Shadow Shield**

Since total flux levels for each fuel loading are virtually the same, the shield design can be done independent of fuel loading. To get marginally accurate results, cell thickness of 3 cm with increasing neutron importance of a factor of two were modeled in the shield. In order to achieve lifetimes of 5 years, required neutron dose levels to be below  $10^{13}$  n/cm<sup>2</sup> immediately behind the reactor and  $10^{11}$  n/cm<sup>2</sup> 10 m away from the shield. Based on the MCNP results this required a LiH thickness of 120 cm. Due to the large thickness of LiH, it was found that the energy deposition in lead immediately following the LiH was already below lifetime thresholds. Therefore, only the LiH shield was needed. Figure 5-12 shows the orientation of the LiH shield with respect to the bottom of the reactor as well as the 11.5 degree angle of protection. Neutron and gamma flux levels exiting the shield were  $10^4$  n/(cm<sup>2</sup>-s) and  $4.3 * 10^{11}$  p/(cm<sup>2</sup>-s) respectively.

### **Closed Cycle Thermal Hydraulic Results**

Table 5-2 shows some characteristic properties of the reactor as well as MHD electrical power for each of the four fuel loadings as well as a constant power profile. As expected a constant power profile provides the best conditions for operation with rubidium exit temperature of 2039 K and a maximum fuel temperature of 2759 K. This corresponds to an electrical power generation of 942 kWe. The 13% fuel, which results in the least favorable operating conditions with respect to MHD power generation has an exit rubidium temperature of 2018 K and a maximum fuel temperature of 2832 K. Figure 5-6 compares the axial temperature distributions for the rubidium and maximum fuel temperatures for the 13% fuel power profile and a constant power profile using the 1-D model. Due to the lower rubidium exit temperature the MHD power

is only 922 kWe for the 13 percent fuel loading. Although the rubidium exit temperature is 21 K lower than the constant power profile exit temperature, the maximum fuel temperature for the 13% fuel is nearly 100 K higher, because the 13% fuel's power profile has a significant peak at the top of the reactor. This extra heat generated at the top of the reactor causes temperatures at the top of the reactor to be much higher for the 13% fuel than for a constant power profile. Variation in uranium concentration could reduce the large fuel temperatures, but the spike in power that is of primary concern is the one at the top of the reactor not at the bottom. As seen in Figure 5-10, the 8% fuel which has the flattest profile with the exception of the bottom spike also has corresponding exit rubidium temperatures and maximum fuel temperatures that are closer to the constant power profile as seen in Table 5-2. By reducing the both spikes at the top and bottom of the reactor, the thermal hydraulic performance would become very close to the conditions generated by a constant linear heat generation rate.

Table 5-3 shows the exit rubidium properties of each component in the closed cycle system when the reactor has a constant power profile, as well as the power associated with each component. Generating 942 kWe of electric power the cycle efficiency is 15.7%. However, approximately 35% of the total thermal power added to the rubidium coolant goes into the heating of the liquid phase and the phase change. Only the remaining 3.9 MWth actually heats the rubidium vapor and it is only from this state that the MHD generator can generate power. Therefore, the MHD generator itself has an efficiency of 24.3%.

Another important quantity in Table 5-3 is the rubidium temperature of 1040 inside the condensing radiator. This high temperature enables over 3 MW of heat to be radiated away over a relatively small area of 50 m<sup>2</sup>.

## Spacecraft Mass and Specific Power

Table 5-4 shows the mass estimates and specific mass for all the components of the spacecraft. The reactor is the single most massive component of the spacecraft with a mass of 2514 kg followed by the PMAD with a mass of 1144 kg. The shadow shield is the next most massive component at 860 kg since over a meter of LiH thickness is required to adequately reduce flux levels. Relative to other spacecraft requiring similar levels of heat rejection, the radiator is quite light requiring a radiating area of only 50 m<sup>2</sup> and a corresponding mass of 739 kg. Finally, the mass of the supporting structure (656 kg) and the mass of the MHD (642 kg) make up the remaining components that significantly contribute to spacecraft mass. The diffuser, pump and nozzle all contribute extremely little mass to the system. Overall, this spacecraft design appears capable of producing 942 kW of electric power with a total mass of 6566 kg (a spacecraft specific mass of 6.97 kg/kWe).

Figure 5-13 shows the fuel usage as well as round trip time as a function of initial fuel mass. A minimum of 728 kg of liquid hydrogen is required for one round trip. Both fuel usage and roundtrip time have a linear relationship with initial fuel mass. Increasing the fuel mass has two primary advantages: increasing the number of ferrying trips before refueling and increasing the amount of shielding from the reactor. The disadvantages include less efficient use of fuel and more time spent in transport mode which decreases the lifetime of the core. In conjunction, with the difficulty in launching very massive refueling payloads it appears the most efficient use of both core power and propellant would be to use propellant refueling loads of 5500 kg. This provides the spacecraft with enough fuel for six round trips with an average trip time of 10.35 days. When considering core burnup, this method of propellant loading results in this spacecraft capable of ferrying 135 GSO satellites before reaching the end of its lifetime.

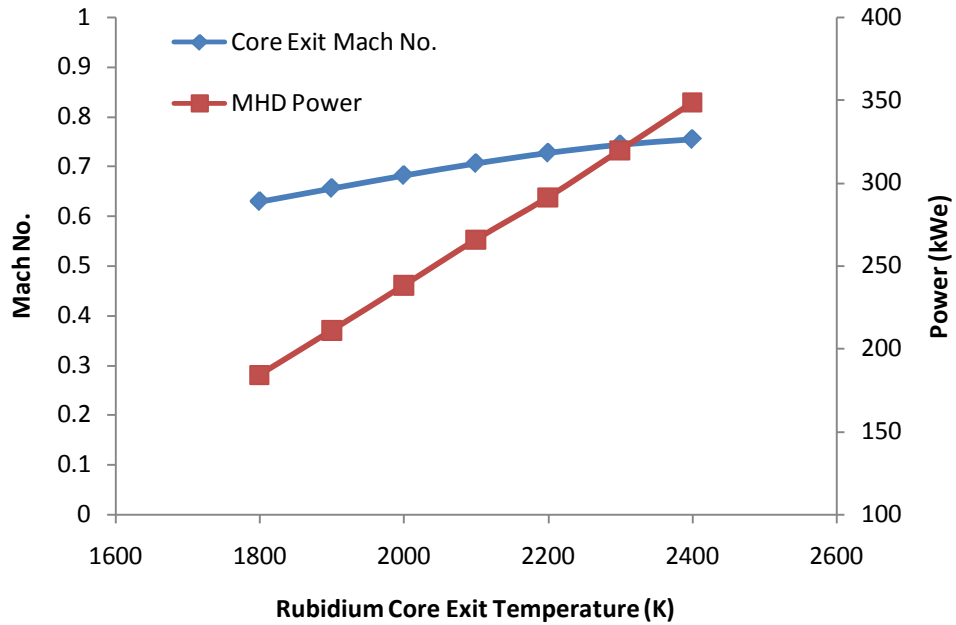


Figure 5-1. Core exit Mach number and MHD for original SLHC design for various core exit temperatures

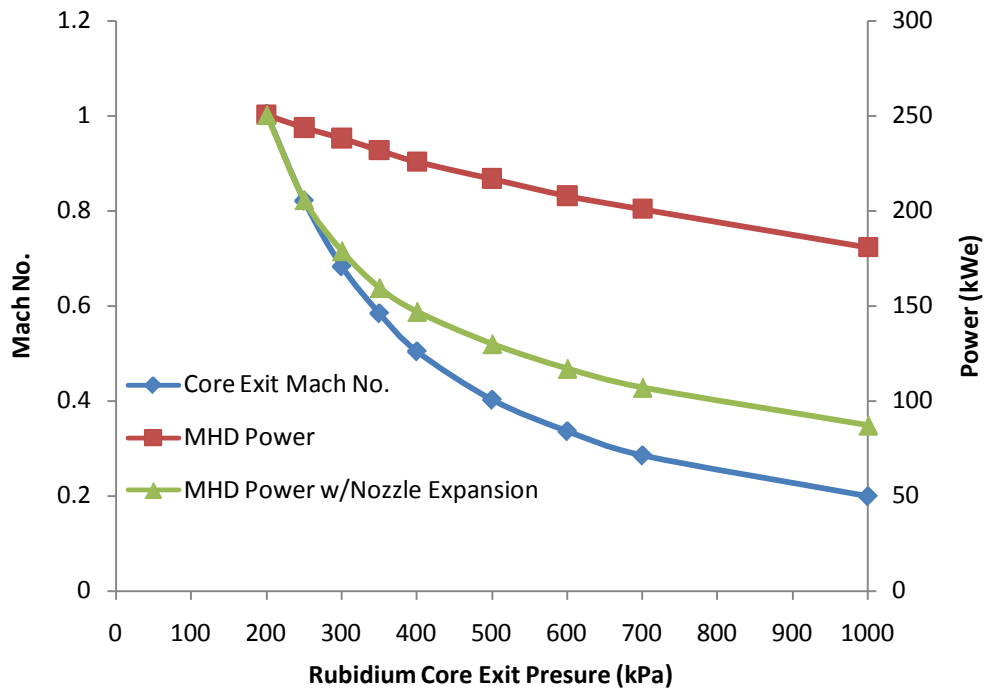


Figure 5-2. Effect of core exit pressure on core Mach number and MHD power both with and without expansion for the original SLHC. Nozzle expands flow to Mach 1.0 before entering MHD generator

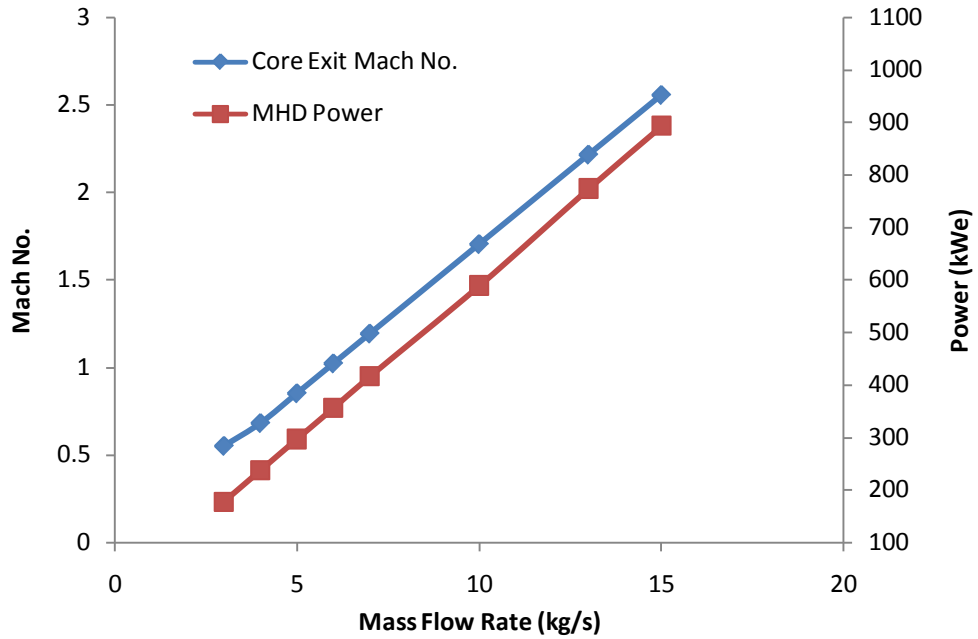


Figure 5-3. Core exit Mach number and MHD power for original SLHC design for various mass flow rates

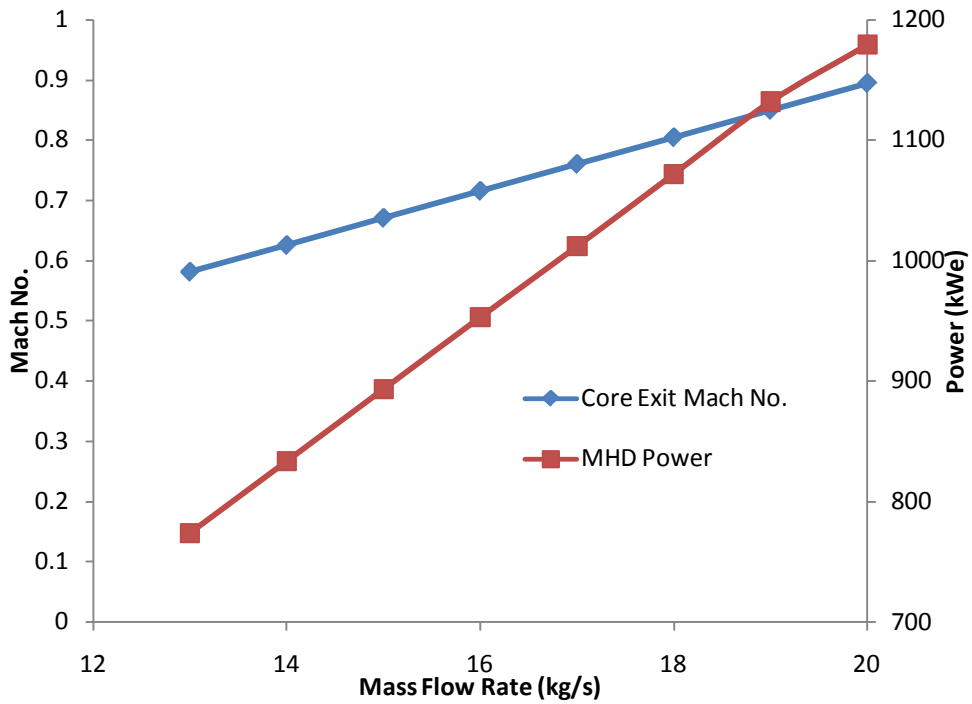


Figure 5-4. Effect of mass flow rate on core exit Mach number and MHD power for the radially-increased SLHC and with 50% cross-sectional flow area within the fuel.

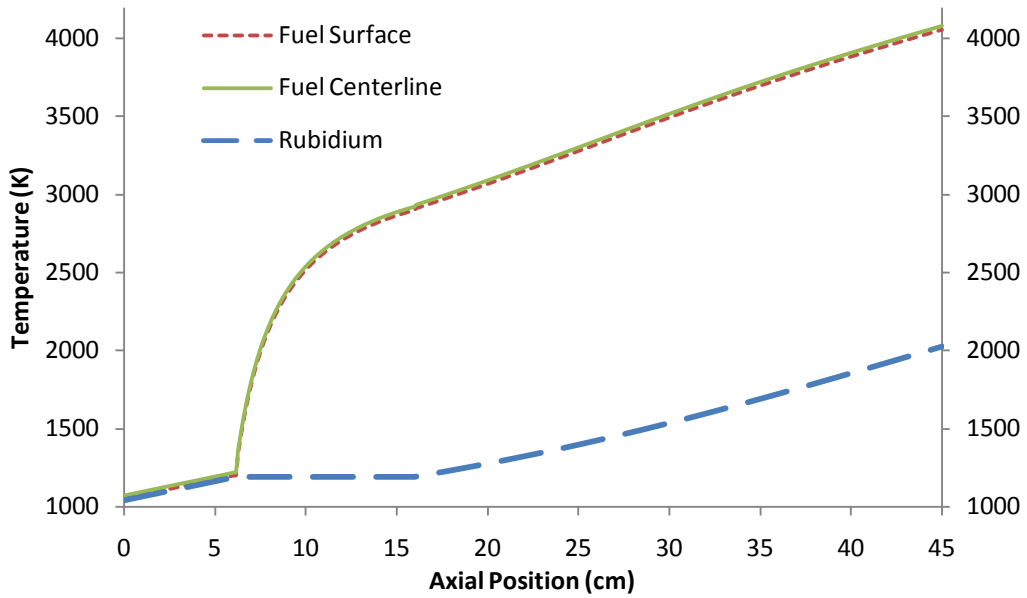


Figure 5-5. Core temperature profiles for radially-increased SLHC with 2 mm fuel wafer thickness for constant LHGR.

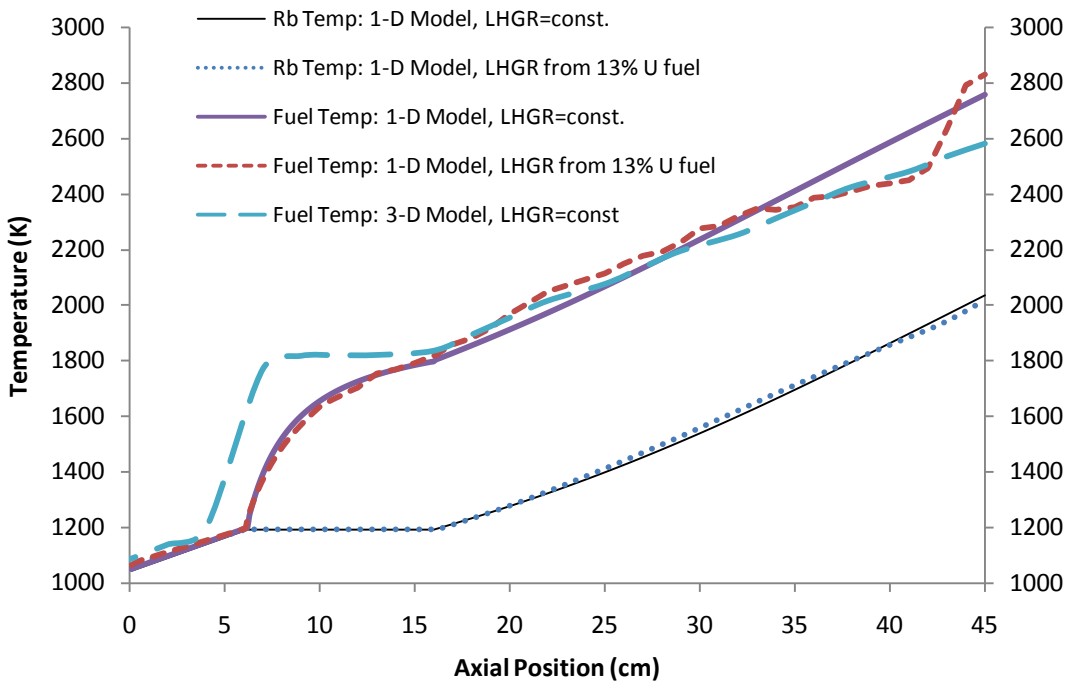


Figure 5-6. Axial core temperatures for radially-increased SLHC with 1 mm thick fuel wafers

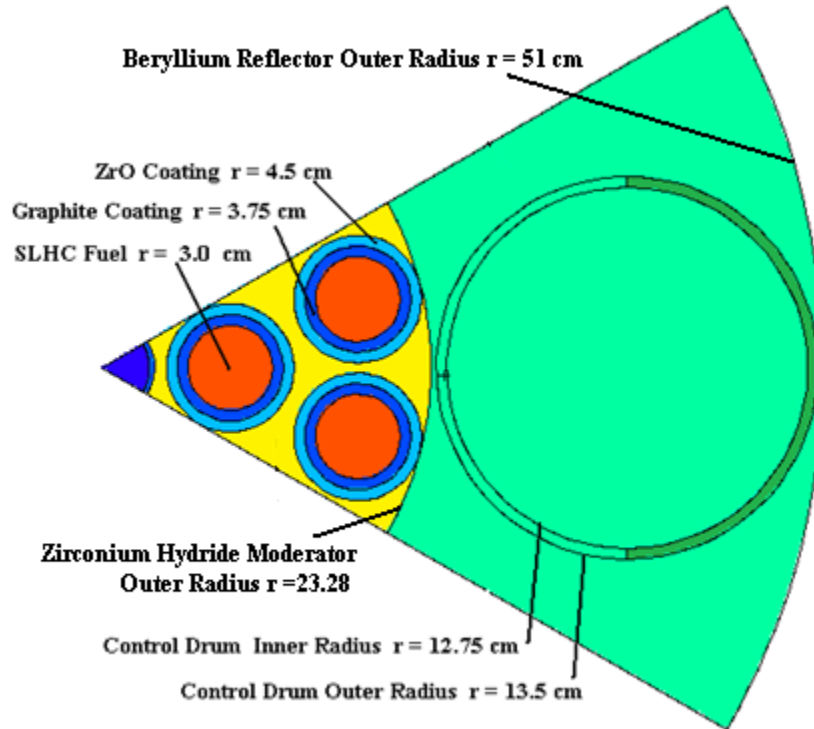


Figure 5-7. Radially-increased SLHC MCNP model

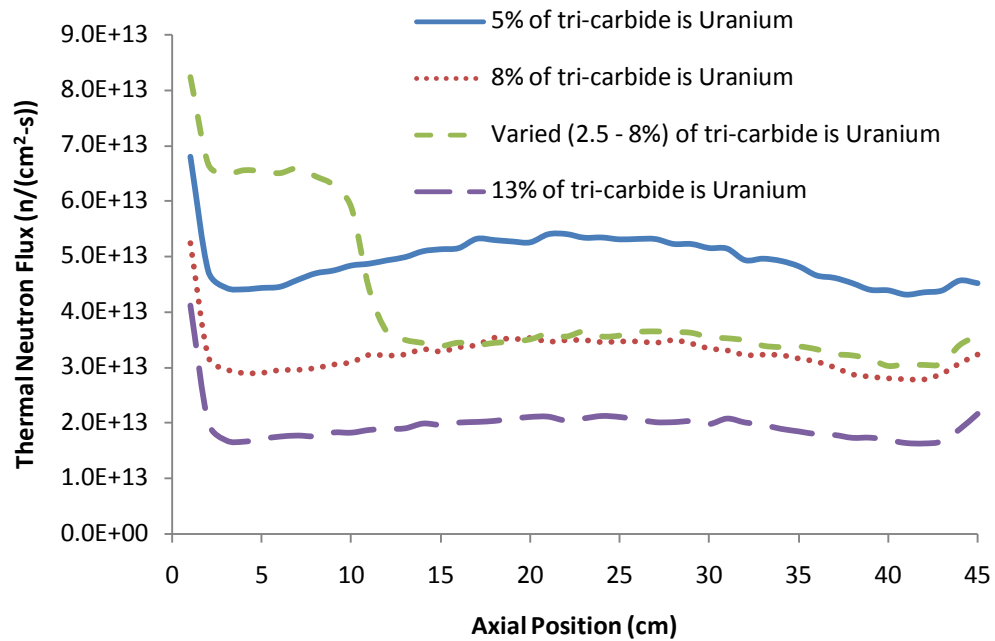


Figure 5-8. Thermal (0 to 1.86 eV) neutron flux for each fuel type at 6 MW

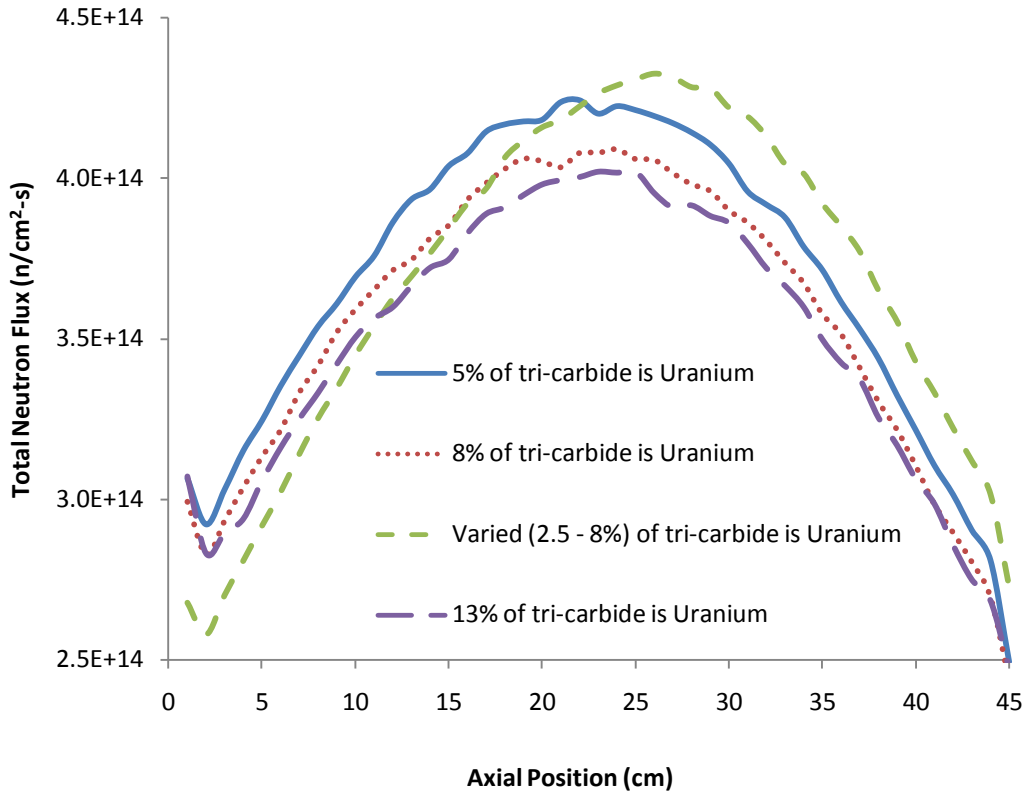


Figure 5-9. Total flux at 6 MW for each fuel type

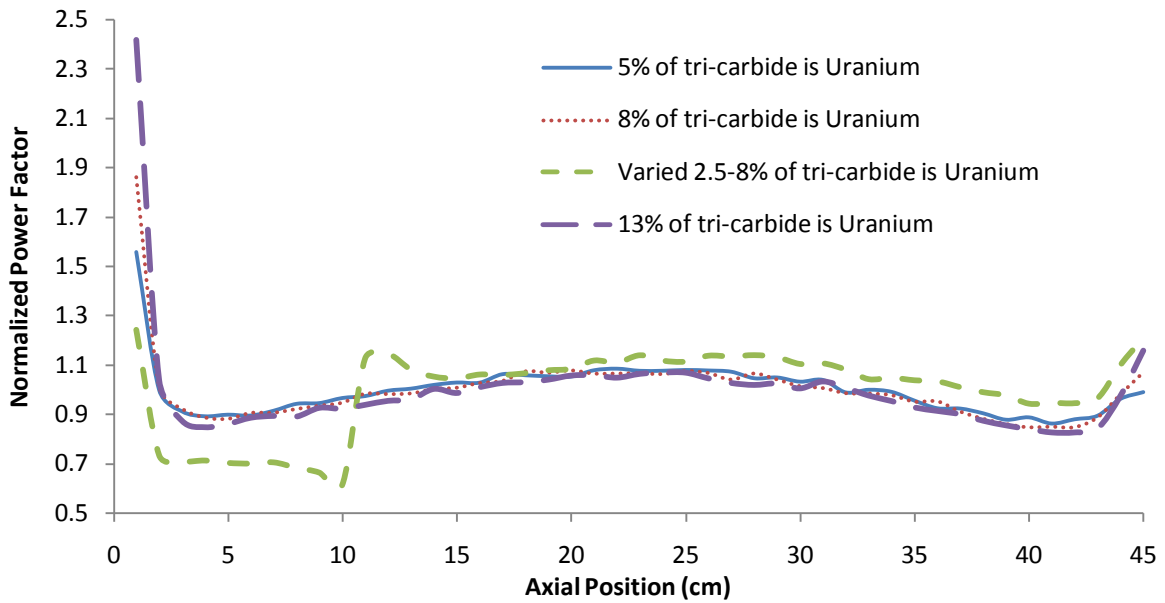


Figure 5-10. LHGR for sub fuel assembly

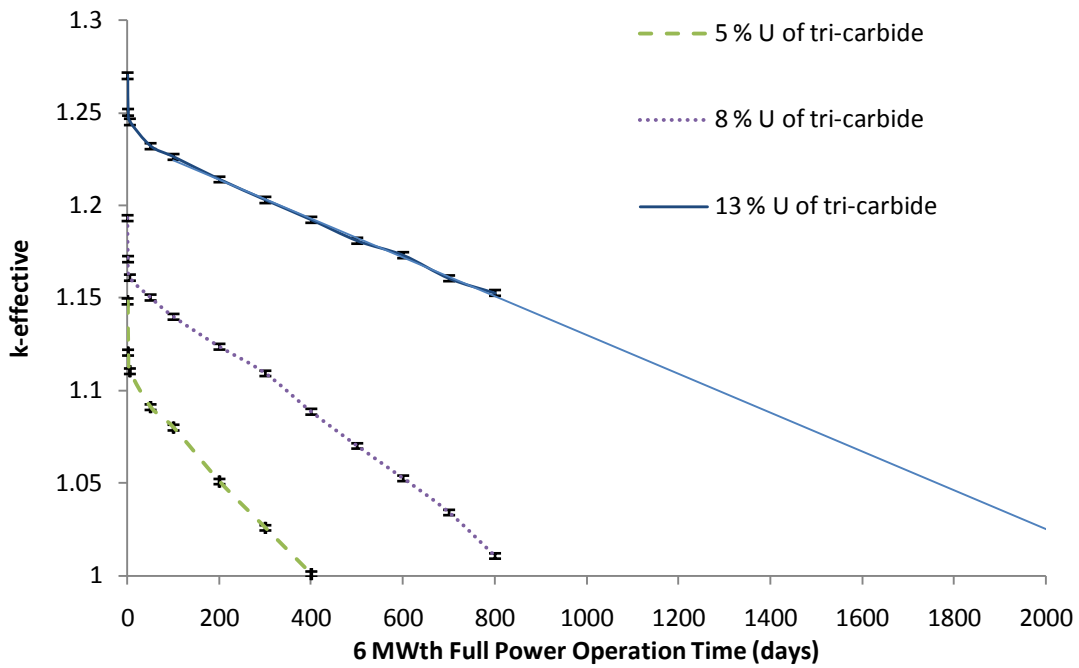


Figure 5-11.  $k_{\text{eff}}$  with fuel depletion for the three different uranium concentrations.

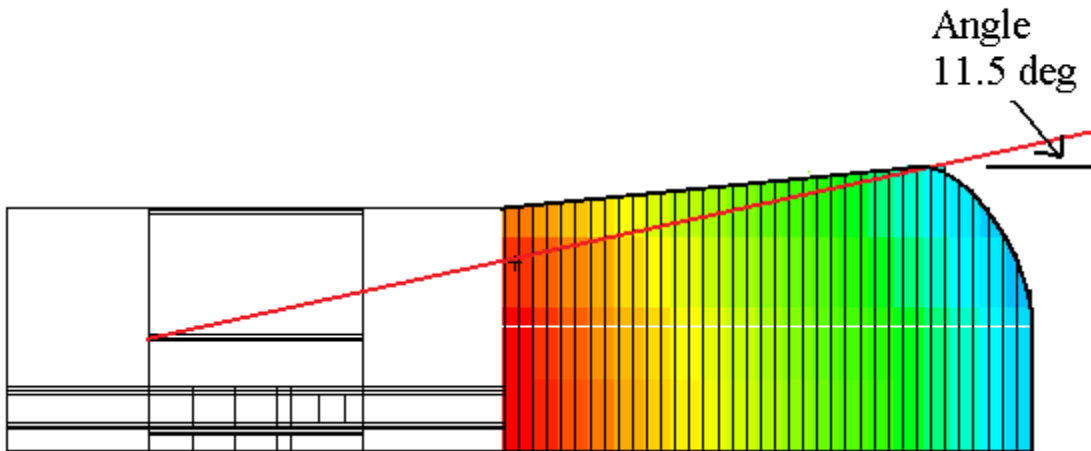


Figure 5-12. LiH shadow shield at the end of the reactor.

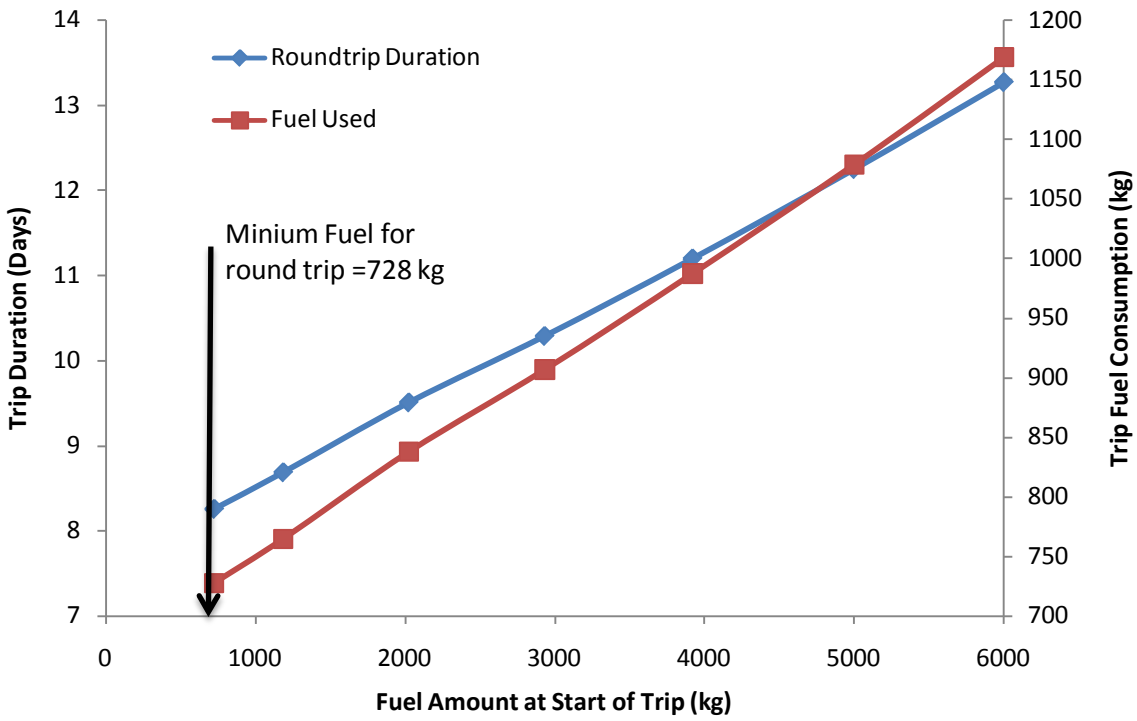


Figure 5-13. LEO to GEO round trip duration and liquid hydrogen consumption vs. starting propellant amount.

Table 5-1.  $k_{\text{eff}}$  both with and without control for different fuel loadings

Uranium Concentration	Control Position	$k_{\text{eff}}$	Relative error
5%	Out	1.14984	0.00048
	In	0.96534	0.00050
8%	Out	1.19532	0.00047
	In	1.01513	0.00051
	Boron Tube	0.86338	0.00050
Varied (5% to 8%)	Out	1.1776	0.00048
	In	0.9984	0.00051
	Boron Tube	0.84746	0.0005
13%	Out	1.26803	0.00047
	In	1.07317	0.00051
	Boron Tube	0.92462	0.00500

Table 5-2. Cycle parameters for various fuel loadings

	Power Profile				
	5% U	8% U	13% U	Varied	Constant
Subcooled Height (cm)	6.4	6.1	6.1	8.4	6.2
Vaporization Height (cm)	16.3	16.1	16.2	17.9	16
Core Exit Temperature (K)	2025	2029.9	2018.1	2039.5	2039.5
Core Exit Pressure (kPa)	293.62	291.24	293.43	315.37	292.98
Core Exit Mach No.	0.69865	0.70549	0.69723	0.65369	0.70375
MHD Power (kWe)	932.25	932.36	922.83	930.48	941.65
Max. Fuel Temp. (K)	2738.8	2800.4	2832.1	2910.3	2759.4

Table 5-3. Cycle component temperature, pressure and associated power

Exit of:	Temperature (K)	Pressure (kPa)	Power (MW)
Core	2039	292	6
MHD	971	115	0.942
Diffuser	1295	247	
Condenser	1040	183	-3.28
Pump	1043	615	0.016

Table 5-4. Mass and specific mass for each system component

Component	Mass (kg)	Specific Mass (kg/kW)
Reactor	2514.6	0.43 kg/kWth
Fuel Sub Assemblies	380	
Moderator	148	
Center Tube	390	
Side Reflector	253	
Control Drum	480	
Axial Reflector	865	
PMAD	1144.0	1.24 kg/kWe
Shadow Shield	860	0.135 kg/kWth
Radiator	739.0	0.23 kg/kWth
Supporting Structure	656.6	0.90 kg/kWe
MHD PC	642.0	0.69 kg/kWe
Diffuser	5.6	0.006 kg/kWe
Nozzle	3.7	0.004 kg/kWe
Pumps	0.4	0.024 kg/kW pump
<b>Dry Spacecraft</b>	<b>6565.8</b>	<b>6.97 kg/kWe</b>
Fuel (initial loading)	5500	
<b>Wet Spacecraft</b>	<b>12065.8</b>	<b>12.8 kg/kWe</b>

## CHAPTER 6 CONCLUSION

### **Thermal Hydraulics**

The use of rubidium in the square lattice honey comb reactor with MHD power conversion appears feasible; however, to generate approximately 1 MW of electrical power required increasing the flow area through the core. The radially-increased core in conjunction with the increased cross sectional flow area allowed for larger mass flow rates without choking the flow inside the reactor. Additionally, the fuel wafer thickness was reduced from 2 mm to 1 mm in order to reduce fuel temperatures from near 4000 K at the exit of the core which are in excess of the 3000 K maximum operating temperature. Optimal flow conditions (2040 K and 292 kPa) for the MHD generator were produced when operated with a flow rate of 15 kg/s and a thermal power of 6 MW. However, cycle efficiencies are limited by the condensation of rubidium vapor within the MHD generator and over half of the total thermal power must be radiated away in the condenser.

Higher power designs are feasible but require increasing the flow area of the reactor. However, radially increasing the core by much more, thereby increasing the fuel within the core, and still maintaining control of the reaction would be difficult without radically changing the design of the reactor.

Thermodynamic data for high temperature rubidium is limited. Additionally, two phase flow studies with rubidium are virtually non-existent. Therefore, the degree of uncertainty for the operating conditions of this reactor is large. However, the thermal hydraulic analysis performed shows that temperatures within the core can be kept below the maximum operating limit which is 800 K below the fuel's melting temperature.

## **Fuel Effects**

Fuel loading with 5% uranium in the tri-carbide fuel provides the best power profile with respect to fuel temperatures but offers full power operation of only 400 days but can still be brought subcritical by the control drums alone. The 8 % uranium fuel loading provides marginal reactor lifetime of 800 days but requires a boron tube at the center of the reactor to control the reaction. The 13% fuel provides adequate reactor lifetime with approximately 5.5 full power years, but has the least desirable axial power profile resulting in the highest fuel temperatures. Varying uranium concentration axially does have dramatic effects on the power profile and by decreasing the concentration of uranium at the top of the reactor maximum fuel temperatures can be decreased. The 13% fuel loading was capable of 5.5 years of full power operation, which in conjunction with propellant loading and number of GSO launches per year, indicates a core lifetime between 7 and 10 years.

## **Mass and Power.**

The mass and power of the spacecraft are very promising at 6566 kg and 942 kWe, respectively. Considering the average GSO satellite has a mass of 4500 kg, the mass of this space transport is manageable with current launch vehicles. Additionally, the use of a disk MHD generator can improve cycle efficiency and reduce the generator mass of the system, making this a conservative analysis of system performance

## **Future Work**

In order to accurately understand what is occurring during the two phase flow, two phase boiling experiments with rubidium need to be done for similar mass fluxes and geometry to those modeled. Also, ionizing experiments with nuclear enhanced rubidium must verify that electric conductivities of 100 mho/m are capable at temperatures between 1000 K and 2000 K. Additionally, this study addresses only the steady state neutronic properties of the core, and has

yet to consider any transient analysis. Along these lines, the effect of void coefficients and the manner in which two phase flow is turbulent could cause severe issues with controlling the reactor and must be analyzed.

APPENDIX  
MATERIAL ISOTOPE CONCENTRATIONS

Fuels	Isotope	Fraction	
		Core Entrance	Core Exit
2.5 % U	Rb-87	4.065E-03	1.609E-04
	C-12	1.263E+01	4.999E-01
	U-235	2.937E-01	1.162E-02
	U-238	2.211E-02	8.749E-04
	Zr-90	5.199E+00	2.058E-01
	Zr-91	1.134E+00	4.487E-02
	Zr-92	1.733E+00	6.859E-02
	Zr-94	1.756E+00	6.951E-02
	Zr-96	2.829E-01	1.120E-02
	Nb-93	2.211E+00	8.749E-02
	Number Density #/(b-cm)	4.332E-02	3.958E-02
5% U	Rb-87	8.662E-02	1.609E-04
	C-12	4.567E-01	4.999E-01
	U-235	2.124E-02	2.325E-02
	U-238	1.598E-03	1.750E-03
	Zr-90	1.880E-01	2.058E-01
	Zr-91	4.099E-02	4.487E-02
	Zr-92	6.266E-02	6.859E-02
	Zr-94	6.350E-02	6.951E-02
	Zr-96	1.023E-02	1.120E-02
	Nb-93	6.850E-02	7.499E-02
	Number Density #/(b-cm)	4.332E-02	3.958E-02
8% U	Rb-87	8.662E-02	1.609E-04
	C-12	4.567E-01	4.999E-01
	U-235	3.398E-02	3.719E-02
	U-238	2.557E-03	2.800E-03
	Zr-90	1.880E-01	2.058E-01
	Zr-91	4.099E-02	4.487E-02
	Zr-92	6.266E-02	6.859E-02
	Zr-94	6.350E-02	6.951E-02
	Zr-96	1.023E-02	1.120E-02
	Nb-93	5.480E-02	5.999E-02
	Number Density #/(b-cm)	4.332E-02	3.957E-02

Fuels	Isotope	Fraction	
		Core Entrance	Core Exit
	C-12	4.567E-01	4.999E-01
	U-235	5.521E-02	6.044E-02
	U-238	4.156E-03	4.549E-03
	Zr-90	1.880E-01	2.058E-01
	Zr-91	4.099E-02	4.487E-02
	Zr-92	6.266E-02	6.859E-02
	Zr-94	6.350E-02	6.951E-02
	Zr-96	1.023E-02	1.120E-02
	Nb-93	3.197E-02	3.499E-02
	Number Density #/(b-cm)	4.332E-02	3.957E-02

Material	Isotopes	Fraction
Zirconium Center Tube	Zr-90	5.145E-01
	Zr-91	1.122E-01
	Zr-92	1.715E-01
	Zr-94	1.738E-01
	Zr-96	2.800E-02
	Density (g/cm <sup>3</sup> )	6.511E+00
ZrH Moderator	Zr-90	1.715E-01
	Zr-91	3.740E-02
	Zr-92	5.717E-02
	Zr-94	5.793E-02
	Zr-96	9.334E-03
	H-1	6.667E-01
	Density (g/cm <sup>3</sup> )	6.690E+00
Beryllium Reflector	Be-9	1.000E+00
	Density (g/cm <sup>3</sup> )	1.850E+00
Graphite Coating	C-12	1.000E+00
		2.820E+00
ZrO Coating	Zr-90	1.72E-01
	Zr-91	3.74E-02
	Zr-92	5.72E-02
	Zr-94	5.79E-02
	Zr-96	9.33E-03
	O-16	6.67E-01
	Density (g/cm <sup>3</sup> )	5.89E+00

---

Boron Carbide	B-10	8.00E-01
	C-12	2.00E-01
	Density (g/cm <sup>3</sup> )	2.51E+01

---

## LIST OF REFERENCES

- Angelo, J. A. Jr., Buden, D., 1985. Space Nuclear Power. Orbit Book Company, Inc., Malabar, FL.
- Anghaie, S., Knight T., 2004. Development of Robust Tri-Carbide Fueled Reactor For Multi-Megawatt Space Power and Propulsion Applications. Transactions of the American Nuclear Society 91, 908.
- Anghaie, S., 2000. Development of Liquid-Vapor Core Reactors with MHD Generator for Space Power and Propulsion Applications In: 8<sup>th</sup> International Conference on Nuclear Engineering (ICONE-8018), Baltimore, Maryland.
- Anghaie, S., Ferrari, A., 2007. Nuclear Enhanced MHD-MPD Thruster. In: International Congress on Advances in Nuclear Power Plant (ICAPP 2007): The Nuclear Renaissance at Work Conference, Nice Acropolis, France.
- Bate, R.R., Mueller, D.D., White, J.E., 1971. Fundamentals of Astrodynamics. Dover Publications, Inc., New York, NY.
- Begg, L.L., Engdahl, E. H., 1989. Advanced Radiator Concepts. In: Proc. 24<sup>th</sup> Intersociety Energy Conversion Engineering Conference (IECEC-89), Institute of Electrical and Electronics Engineers 75-80.
- Bird, B., Stewart, W.E., Lightfoot, E.N., 1960. Transport Phenomena. Wiley, New York, NY.
- Carbajo, J.J., 2005. Applicability of Heat Transfer Coefficient Correlations to Single Phase Convection in Liquid Metal. Oak Ridge National Laboratory, Oak Ridge, TN.  
[http://www.ornl.gov/sci/scale/pubs/ldoc9924\\_comparison\\_of\\_heat\\_transfer.pdf](http://www.ornl.gov/sci/scale/pubs/ldoc9924_comparison_of_heat_transfer.pdf) Retrieved Jan. 2009.
- Galabova, K. et. al., 2003. Architecting a Family of Space Tugs Based on Orbital Transfer Mission Scenarios. *AIAA Space*. Paper 2003-6368.
- Gouw, Reza 2005. Nuclear Design Methodology for Analyzing Ultra High Temperature Highly Compact Ternary Carbide Nuclear System. Dissertation. University of Florida Department of Nuclear and Radiological Engineering.
- Hendricks, John et al., 2007. MCNPX Version 26D. Los Alamos National Laboratory, Los Alamos, NM.
- Kandlikar, Satish ed., 1999. Handbook of Phase Change: Boiling and Condensation. Taylor and Francis, Ann Arbor, MI.
- Litchford, R.J. et al., 2001. Prospects for Nuclear Electric Propulsion Using Closed Cycle Magneto Hydrodynamic Energy Conversion. NASA Marshall Flight Center. Huntsville, <http://ntrs.nasa.gov/search.jsp> Retrieved Jan. 2009.

- Maya, I.A., Anghaie, S., Diaz, N.J., Dugan, E.T., 1993. Ultrahigh Temperature Vapor-core Reactor: Magnetohydrodynamic System for Space Nuclear Electric Power. *Journal of Propulsion and Power* 9, 98.
- Metcalf, K. J., 1993. Power Conditioning System Modeling for Nuclear Electric Propulsion. NASA Contractor Report. CR-191136.
- Mitchner, M., Kruger, C.H. Jr., 1973. *Partially Ionized Gases*. John Wiley & Sons, Inc, New York, NY.
- NASA Glenn Research Center. Magnetoplasmadynamic Thruster. 2008. <http://www.nasa.gov/centers/glenn/about/fs22grc.html> Retrieved Feb. 2009.
- Neuer, G., 1995. Spectral and Total Emissivity Measurements of Highly Emitting Materials. *International Journal of Thermophysics* 16, 257.
- Pelowitz, D. ed., 2005. MCNPX User's Manual: Version 2.5.0. Los Alamos National Laboratory, Los Alamos, NM.
- Rosa, R.J., 1968. *Magnetohydrodynamic Energy Conversion*. Hemisphere Publishing Corp, New York.
- Futron Corporation. Space Transportation Costs: Trends in Price per Pound to Orbit 1990-2000. 2002. [http://www.futron.com/pdf/resource\\_center/](http://www.futron.com/pdf/resource_center/) Retrieved Oct. 2008.
- Stavros A. et al., 2001. Dimensionless Correlations for Forced Convection in Liquid Metals: Part 1 Single Phase Flow. *Metallurgical and Materials Transactions B*. Vol. 32B, 245.
- Todreas, N. E., Kazimi, M. S., 1990. *Nuclear Systems I: Thermal Hydraulic Fundamentals*. Taylor and Francis Group, New York.
- Tong, L. S., Tang, Y. S., 1997. *Boiling Heat Transfer and Two Phase Flow*. 2<sup>nd</sup> Ed. Taylor and Francis Group, Washington D.C.
- Vargaftik, N. B., 1975. *Handbook of Physical Properties of Liquids and Gases: Pure Substances and Mixtures*. 2<sup>nd</sup> Ed. Hemisphere Publishing Corp., New York.

## BIOGRAPHICAL SKETCH

Arlo Jeffrey Swallow was born in 1984 in Elko, Nevada. Upon graduating Spring Creek High School as valedictorian in 2003, Arlo entered the United States Naval Academy for his undergraduate education. While attending the United States Naval Academy, Arlo majored in astronautical engineering and also led many of his peers as 20<sup>th</sup> Company Commander. In 2007, Arlo Swallow graduated with distinction from the United States Naval Academy earning a Bachelor of Science degree. Arlo received a Master of Science degree in nuclear engineering from the University of Florida in May 2007. Arlo Swallow returned to U.S. Navy to complete submarine training in Charleston, SC in June of 2007.